Evaluation of Protruding Centerbody on the Novel Airdata Sensor

BY

Adrian Kok Chiang Lee

Submitted to the graduate degree program in Aerospace Engineering and Graduate Faculty of the University of Kansas in partial fulfillment of the requirements for the degree of Master of Science.

_____
Dr. Ray Taghavi, Chairperson

Committee Members: _____
Dr. Saeed Farokhi

_____
Dr. Shawn Keshmiri

Date Defended: May 9, 2016

The Thesis Committee of Adrian Kok Chiang Lee certifies that this is the approved version of the following thesis:

Evaluation of Protruding Centerbody on the Novel Airdata Sensor

_____
Dr. Ray Taghavi, Chairperson

Committee Members: _____
Dr. Saeed Farokhi

_____
Dr. Shah Keshmiri

Date Defended: May 9, 2016

Abstract

A novel airdata sensor was developed at the University of Kansas[1]. The Bio-Inspired probe was designed for high angles of attack and sideslip use, suitable for Unmanned Aerial Vehicle (UAV) flight control system and other highly maneuverable aircraft applications. The probe displayed excellent speed measurement of up to angle of attack and sideslip of ±40°, compared to ±25° exhibited by a conventional pitot tube at the same accuracy.

With the goal of evaluating the novel probe's protruding centerbody and effects on angular sensitivity, two new sets of probe were developed, featuring elongated (L/D 1.5) and shortened (L/D 0.5) protruding centerbodies to gain deeper understanding of the Coanda effect on the blunt protruding centerbody featured on the Bio-inspired probe. The protruding centerbody uses the Coanda effect to turn air flow streamline and attach to the centerbody surface. The analysis included pressure and velocity measurement at high angle of attack wind tunnel tests and Computational Fluid Dynamic simulations on the new and original (L/D 1.0) prototypes. As expected, the elongated ellipsoid centerbody (L/D 1.5) probe exhibited an improved flow capture. Design improvements such as centerbody optimization and direct drag measurement are suggested to improve the novel probe capabilities. Further research will be concentrated on a flight testing on a UAV with the novel airdata sensor and a conventional Pitot-static tube.

Acknowledgement

A special thanks goes to Dr. Taghavi, Dr Keshmiri and Dr. Farokhi for the thoughtful guidance and education insights during my time at the University of Kansas. Dr. Taghavi for his advises for both durations of my bachelor and master degrees, Dr. Farokhi for his ever impressive classes in propulsion and Dr. Keshmiri for his passion to see his students succeed. I am grateful for all their patience, dedication to impart all the knowledge they have in me and inspiring me to do the same to others.

I also want to thank Dr. Ron Barrett and Dr. Richard Bramlette and for their technical support in the wind tunnel lab and on 3-D model printing. Dr. Barrett specifically, for his wonderful class in aircraft design and reminding me how cool aircraft design and history is over the decades.

Last and certainly not least, I want to thank God, family, colleagues and friends for their unceasing love, fellowship and encouragement during my time in Lawrence, Kansas, has reminded me of my responsibility and to continue to challenge me to make a difference in the world.

Table of Contents

List of Figures

List of Tables

List of Symbols

Symbol	Description	Units
C_D	drag coefficient	~
D	probe outer diameter	in
D’	drag	N
L	length of the protruding centerbody	in
P	gage pressure	Pa
P_0	static pressure	Pa
P_t	total pressure	Pa
$\bar{q}$	dynamic pressure	Pa
V	wind speed	ft/s
α	angle of attack	deg
β	sideslip	deg
θ	flow angle	deg

Acronyms

CFD	Computational Fluid Dynamics
DAQ	Data Acquisition
RANS	Reynolds-averaged Navier-Stokes equation
UAS	Unmanned Aircraft Systems
UAV	Unmanned Aerial Vehicle

1 Introduction

With the increased use of UAS in flight research, there is a need to improve the onboard airdata sensor instrument that is compact and reliable and has the ability for on-board simultaneous data input and yield.

The novel airdata sensor is designed for simultaneous measurements of total and static pressure and total temperature of a streaming gas flow with improved flow angularity capture capability[1]. Inspired from the Peregrin Falcon (Figure 1), the Bio-Inspired probe (see Figure 2) featured an axisymmetric body that protrudes outside, forward of the elliptical lip (contoured) of the hallowed tube that allows wide angular flow capture[2]. The protruding centerbody is based on the Peregrine falcon's cone shape bone in its nostril called baffles, seen on Figure 1. The baffles allowed air to flow into the nostril at diving speed of 200mph, where shock wave would have block airflow. This incredible nature design inspired the protruding centerbody design, thus the probe name 'Bio-Inspired.'

Figure 1: Peregrine falcon[3]

Air flow is captured by the blunt axisymmetric centerbody that protrudes out forward of the probe through the use of Coanda effect, enhancing the flow sensitivity of the probe. The Coanda effect, coined by Henri Coanda in the 1930s, is a phenomena where moving fluid flow attaches and follows a solid surface (i.e. airfoil, flat plate or streamline body)[4]. To ensure a throughflow inside (through the outer sleeves), the probe is designed with an aft vent that helps angular flow to enter the probe, thus enabling the capture and conversion of the flow's lateral energy into dynamic pressure[1]. Further additions of micro vortex generators on the protruding

centerbody improves flow capture and attachment at high flow angularity. The vortex generators are arranged on the centerbody surface in a certain way which creates a textured skin, much similar to a shark skin[5]. Stagnation pressure and temperature of the flow are measured at the aft stagnation tube in the probe. In addition to the pressure and temperature measurement, the protruding hallow centerbody can include miniaturized IMUs and other suite of sensors.

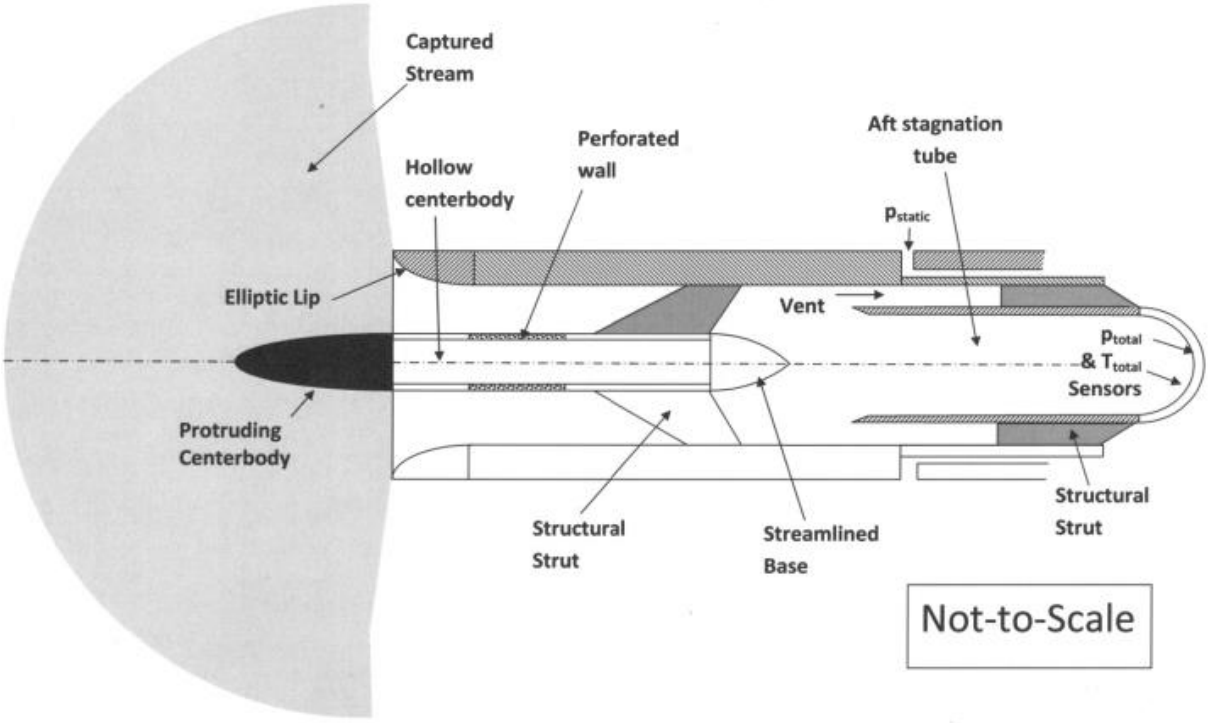

Figure 2: Novel probe characteristic and design[1]

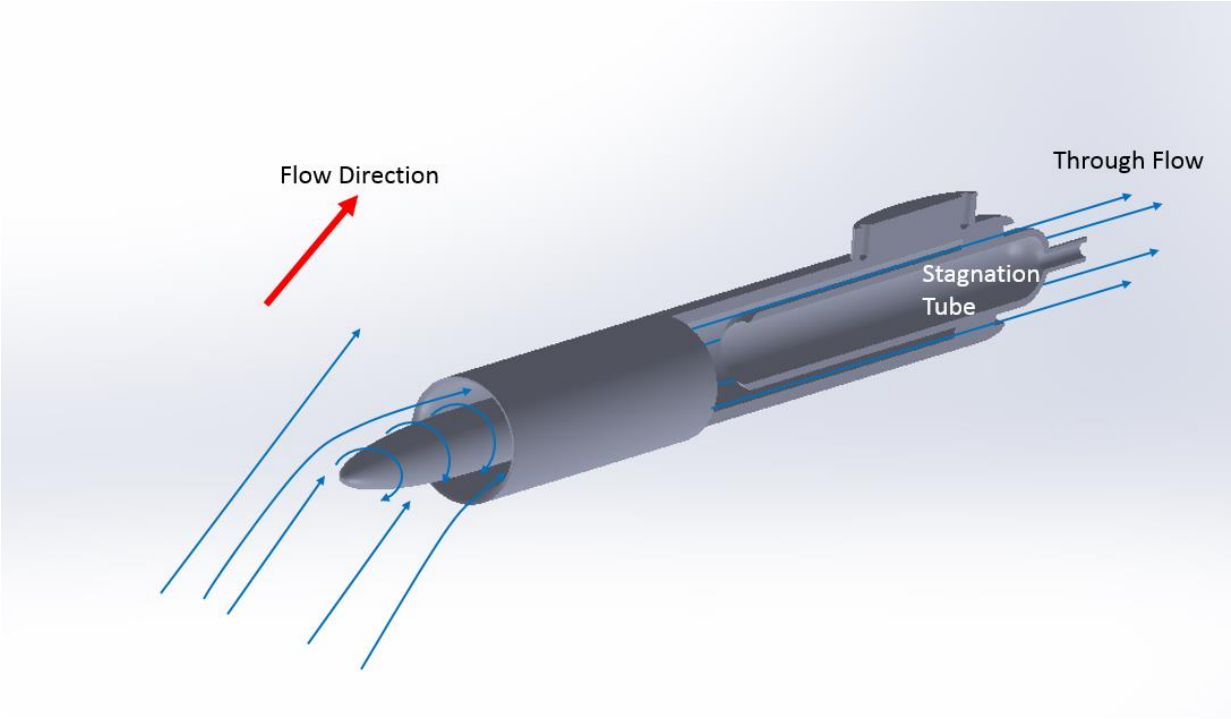

Figure 3: Angular flow attachment on protruding centerbody by Coanda effect[6]

The novel probe houses at least three sensors that measure static and total pressure and temperature. These inputs are channeled to an on-board microprocessor, calculating eight mean flow and local fluid parameters, such as Mach number, Reynolds number, fluid static temperature, entropy, fluid density, flow dynamic pressure, flight speed, and local speed of sound. Time-resolved flow data, turbulence intensity, and scale can then be measured using high frequency response piezoelectric pressure

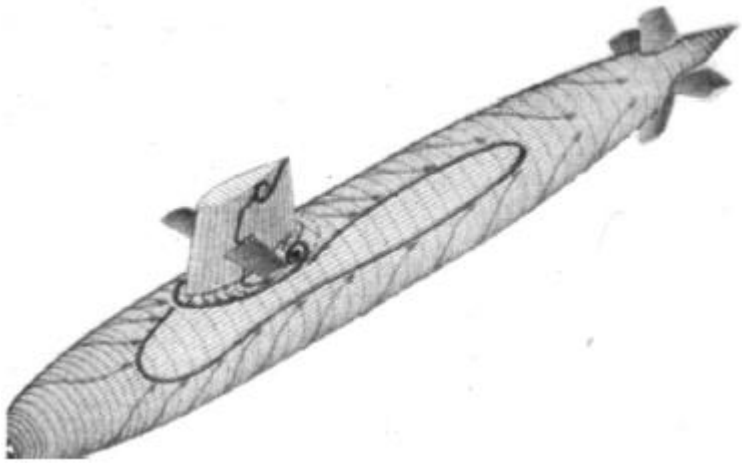

Figure 4: Flow visualization and flow separation on surface of an attack submarine at 20° angle of attack and 10° yaw[6]

transducers and thin-film temperature sensors, allowing the use of time-series data for cross correlation parameters.

The study of Coanda effect on blunt body where flow attaches and bends was undertaken at the University of Kansas back in 1997 using a model attack submarine[6]. Surface flow visualization on the model submarine, at an angle of attack of 20° and a sideslip of 10°, illustrates the Coriolis Effect seen on Figure 3, showing flow bending and wrapping around on the submarine. Learning from this experience, the probe centerbody is designed similarly to the configuration of the submarine.

Scope of Study

The goal of the thesis is to determine the angular sensitivity of the novel probe by the comparison of the probe's total pressure and velocity measurement to a conventional Prandtl pitot-static probe and optimizing the geometry of the novel probe's protruding centerbody.

Chapter 2 will summarize a literature review on air data sensor technology and computational analysis investigation. Chapter 3 explains in detail the Bio-Inspired probe prototype for experimental testing, the parameter used to optimize the probe's protruding centerbody. STAR CCM+ CFD simulations set-up and results will be covered in Chapter 4. Chapter 5 will included theoretical concepts, experiment set-up and procedure, data acquisition, and wind tunnel results. Chapter 6 presents the summary and conclusion of the evaluation and future works.

2 Literature Review

Airdata sensor probes have always been an essential equipment on board aircraft since the beginning of flight. The two most widely use of airdata probe are the Pitot tube and Kiel probe. In recent years, major studies and improvements have been carried out to improve flow data measurements and air data sensor technology for both military and commercial use.

As computational modelling has become prevalent, CFD tool will be used to simulate pressure in the stagnation tube of the novel probe. However, due to the nature of the probe geometry, numerical computation of complex 3-D turbulent flows are to be subjected to swirl and rotation forces on probe's protruding centerbody. Flow separation is also prevalent especially at high angle of attack, α, or sideslip, β, which are currently still subject to being investigated.

Since the literature review will be covering probe technology and CFD simulation, the chapter is therefore conducted in two separate sections: 1) investigating accurate flow measurement and advanced techniques used in air data sensor technology, and 2) CFD investigation.

2.1 Current Air Data Sensor Technology and Advanced Techniques for Accurate Flow Measurement

Dryden Research Facility of NASA Ames Research Center[7] conducted an evaluation on the accuracy of airdata measurements made with hemispherical flow-angularity probe and with a fuselage-mounted pitot-static-pressure probe mounted on a Grumman F-14 Tomcat as part of a high-angle-of-attack flight test program. The evaluation was conducted from an angle of attack of 0° to 63° and sideslip from -22° to 22°, at Mach number 0.3 to 1.3.with the use of a calibrated combined pitot-static and flow-angularity probe for reference. The hemispherical flow-angularity probe measured with good accuracy and only suffered errors at no more than 2°. The pitot-static-

pressure probe showed great sensitivity to changes in angles of attack and sideslip. However at above Mach number 0.87, pressure measurements resulted in inaccurate data.

NASA[8] developed and tested a system to calibrate airdata probes at angles of attack between 0° to 90°. The airdata probe has a swiveling head on a Pitot-static tube. It is designed to provide convenient and inexpensive airspeed calibration for the F-18 High Alpha Research Program (HARV). The test concluded, that the experimental probe is better at approximating airspeed than earlier NACA probes. Currently, the Space Age Control Company[9] developed the same airdata system that is used to calibrate the prototype Bio-inspired probe in wind tunnel test as seen in Figure 5.

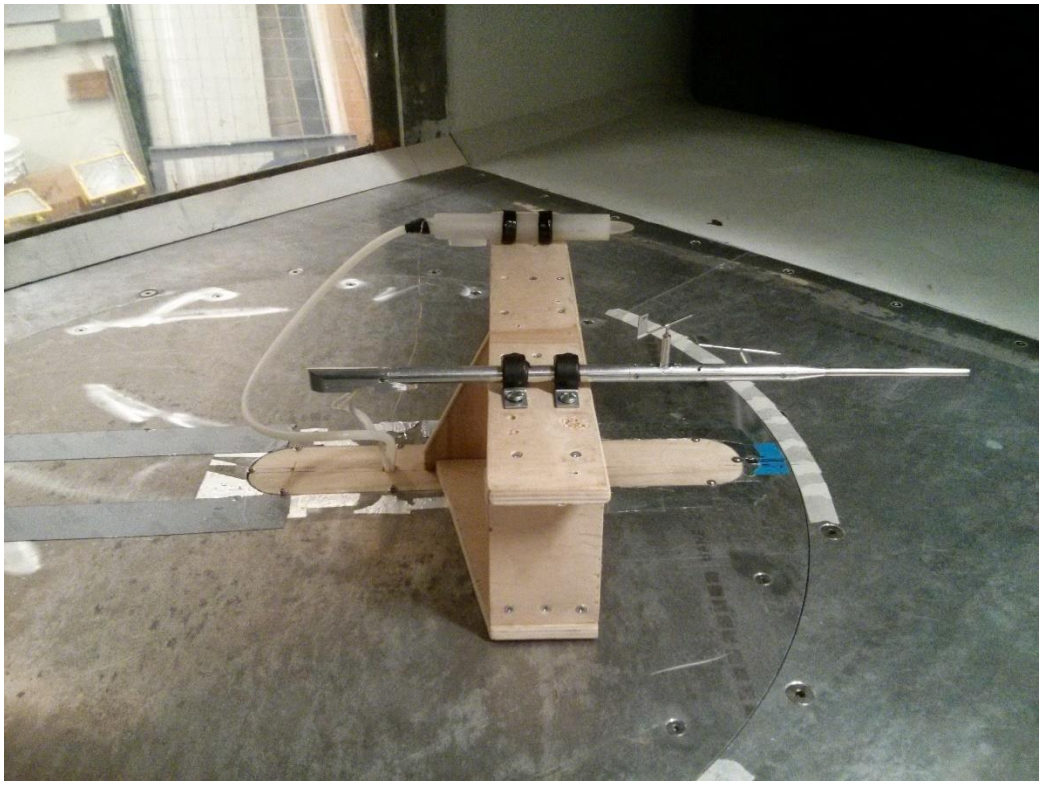

Figure 5: Alpha-beta vane airspeed probe (foreground) and Bio-Inspired probe on calibration stand

NASA installed a non-intrusive high-angle-of-attack Flush Airdata Sensing system (HI-FADS) on the HARV with the goal of obtaining an accurate pressure measurement at high flow

angles. The system consists of a matrix of 25 pressure orifices arranged in concentric circles on the nose of the F-18 vehicle. The test is carried out at an angle of attack ranging from -8° to 55° and sideslip angle of -15° to 15°, and at Mach number of 0.15 to 1.20. During the course of the flight test, it was determined, that satisfactory data can be collected with symmetric use of only 9 ports. Under moderated maneuvering conditions, the HI-FADS gives excellent results[10] [11].

A laser-based airdata measurement sensor has been developed by Ophir Corporation. Ophir's system includes transceivers for projecting laser energy as laser radiation into the air. As the projection expulse into the air, energy will then backscattered from the air and then received by transceivers, producing airdata measurements[12].

Another laser-based airdata system is being develop by Michigan Aerospace Corporation. The Molecular Air Data and Clear Air Turbulence (MADCAT) uses Ultraviolet LIDAR technology to send and received molecular backscatter in the air. It is capable of predicting Clear Air Turbulence (CAT) and full air data measurement, such as airspeed, angle of attack, sideslip, pressure and temperature. Their current proposal is under phase I project of NASA's Small Business Innovation Research / Small Business Technology Transfer (SBIR/STTR) programs focus on combining the two capabilities into a practical solution[13].

Mansour, at ETH Zurich, describes a fast response entropy probe (FENT), developed to document the loss of energy generation in turbomachines. The FENT consists of a Piezo-resistive sensor and a pair of thin-film gauges that is capable of measuring unsteady pressure and temperature. Tested in a centrifugal compressor and axial turbine test rig in the ETH Zurich's turbomachinery facilities, the FENT produced satisfactory results, including up to 48 kHz frequency response[14].

2.2 CFD Investigation

Simulating a 3-D flow across a geometry is no easy task, especially across a complex geometry of the novel probe. Many flow effects needed to be taken in account before setting up CFD simulations to test the ability of the probe. To achieve best CFD results, it is important to understand how the flow would interact with the novel probe's protruding centerbody (i.e swirls, curvature, and vortices).

Earlier works on boundary theory during the 20th century by Hermann Schlichting[15], gave great details of flow regime over a cylindrical body (e.g. flow separation, laminar vs turbulent), depending primarily on Reynolds number. His work was summarize by Holloway[16] in the following: For $Re < 40$, entire flow is laminar and have attach vortices downstream. For $40 < Re < 300$, flow is laminar but have unsteady Karman vortex downstream of the cylinder. At subcritical range, $300 < Re < 1.3 \times 10^5$, boundary layer remains laminar and separates at 80° of the cylindrical body. Downstream wake exhibit turbulent and unsteady behavior. In this regime, laminar boundary layer separates, transition to turbulence, reattaches and separates again, producing turbulent wake. Critical regime of flow over smooth cylinder extends over $1.3 \times 10^5 < Re < 3.5 \times 10^6$.

A study of flow control comparison over an ogive slender nose body, similar to Bio-Inspired probe's centerbody was done by the University of Toledo. The research illustrate a comparison between the elliptical and hemispherical noses, on vortex shedding and side force. Results showed that the ogive nose has good flow reattachment characteristic and generate much easier to control vortices. It is noted that, significant side force is present at 15°-20° angle and huge side-force fluctuation beginning at a yaw angle of 40° showed that flow instability increases

at higher flow angles. It can be determine that, flow separation will start at 40° flow angle onward[17].

A comparative study of turbulence models performance was done by El-Behery and Hamed[18], where thery examined turbulent flow performance in a planar asymmetric diffuser. The physics model used was a steady state Reynolds Average Navier Stoke (RANS) equations for turbulent flow. 6 turbulent models were selected and used for the test. Five of the turbulence models are embedded code, available directly from ANSYS Fluent software (Standard K-Epsilon, Low Reynolds Number K-Epsilon, Standard K-Omega, SST K-Omega and Reynolds Stress Model). Another User Define Function (UDF) code was added. The UDF code is a simplification of the elliptic relaxation Reynold stress model, called v^2-f (V2F) Turbulence model. Compared to experimental results, the UDF code (V2F) performs better than the other 5 turbulent models. This is followed by Standard K-Omega and SST turbulent model. Standard K-Epsilon and Low Reynolds K-Epsilon provide very poor results. The Reynolds Stress model gives unexpected poor results when compared to V2F, K-Omega and SST models.

Although standard one and two equation turbulence models are the workhorse of industrial CFD, native formulation is insensitive to rotation and curvature. Changes are needed on the RANS equation to fully account for flow separation and swirling flow. Holloway[16] proposed that Reynolds stress transport (RST) model could account for the effects of streamline curvature, but would still lack ability to predict the important effects of transition.

Farokhi and Cheng[19] did an investigation in effects of streamline curvature and swirl on turbulent flows on a two dimensional backward-facing step geometry and a two-dimensional S-bend duct geometry. Techniques were developed for improving numerical predictions on turbulent flows with the effects of streamline curvature. Their proposed eddy-viscosity

formulation, improved numerical prediction capability of the standard k-ε model in terms of generality, convenience, and efficiency. However for longitudinal curvature investigation, results show that the standard k-ε model failed in capturing flow separation on the convex surface of the s-blend geometry. It was revealed that larger eddy viscosity along inner surface of the s-blend geometry produced by the k-ε model prevented the occurrence of flow separation. Smaller eddy viscosity model may enable curvature correction and natural onset of flow separation.

The Boeing Company at St. Louis, Missouri[20], did a rotation and curvature correction assessment for one and two-equation turbulence models. Spalart and Shur proposed a rotation and curvature (RC) correction function applicable to both one- and two-equation models. While applied to the one equation model (Spalart-Allmaras turbulence model), it demonstrated to be quite competitive to the advance RST models.

Holloway at Clemson University[16], did a study on unsteady and separated boundary layer prediction over a blunt body using laminar, turbulent and transitional flow. The case study focuses on an unsteady RANS-based CFD physic model to predict separation over a blunt body for a wide range of Reynolds numbers, particularly the ability to capture laminar to turbulent transition. Three turbulent models were used, which are the standard and realizable forms of k-ε model, and newly developed eddy-viscosity model. The eddy-viscosity model is capable of resolving boundary layer transition. Surprisingly, the results of all three models produced an accurate flow regimes in subcritical, critical and supercritical conditions. Discrepancies still existed between experimental and computational results, most likely resulted from turbulent wake in three dimensional flowfield at subcritical and critical Reynold numbers.

2.3 Conclusions summary for CFD simulations

1. Flow in probe would be turbulent, turbulent model needed for accurate data measurement.
2. Swirl and curvature flow effect will hamper accuracy of factory standard turbulence model results.
3. Eddy viscosity formulation needed to correctly predict pressure measurement at higher angle of attack due swirl and curvature effect
4. Using the flow regime summarized by Holloway, flow simulation across the novel probe will be turbulent. Refer to Chapter 4.4 for Reynolds number calculation.
5. One and two equation turbulent models are not adequate to deal with measurements at higher flow angle.
6. Reynold Stress Transport Model may be adequate and accurate but is time intensive and have convergence problem.

3 Bio-Inspired Probe Prototype

The prototype novel probe is manufactured in one piece using stereo lithography process and Accura 60 polycarbonate. The full side and top view of the prototype Bio-Inspired probe can be seen in Figure 7. The centerbody is an ellipsoid with a diameter of 0.5 in. The outer extension of the protruding centerbody (head) from the probe's inlet is 1 inch, making an ellipsoid revolution of L/D 1.0. The elliptic inward lip contour has a major axis to minor axis of 3. The trailing edge of the centerbody is shape into a streamline end to avoid boattail drag. The aft module of the probe house a central tube that can be connected to a pressure sensor.

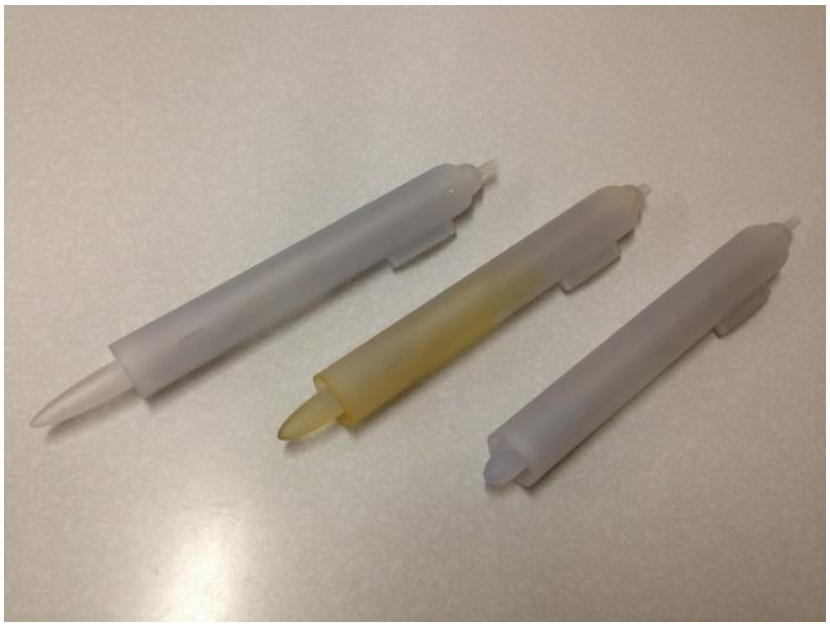

Figure 6: Bio-Inspired Probe Prototypes (Left: L/D 1.5, Mid: L/D 1.0, Right: L/D 0.5)

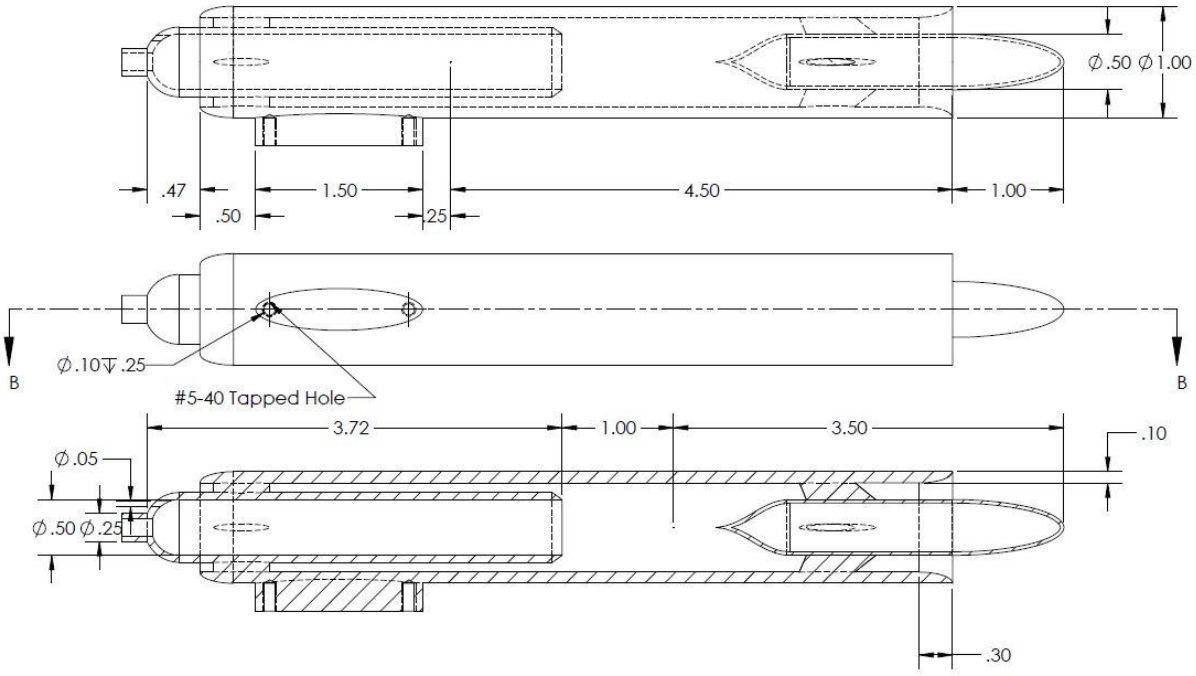

Figure 7: Dimension of Prototype Bio-Inspired Airspeed Sensor Probe

Since this experiment is to perform a parametric study of the probe centerbody, several changes were made to the original design. Static ports and vortex generator seen on Figure 2 were removed. The probe is shortened by one inch since the space to house additional sensors are not needed in the wind tunnel test. The aft open vent that allow through flow in the probe remains, as it is an essential feature of the novel probe. Angular flow would attach to the centerbody, thus increase the accuracy of total pressure measurement at higher flow angles[1].

Two additional probes with a different centerbody ellipsoid revolution 'head' of L/D 0.5 and 1.5 were manufactured to fully test the effects of probe's protruding centerbody length to the pressure measured. The different front assembly side view is shown on Figure 8.

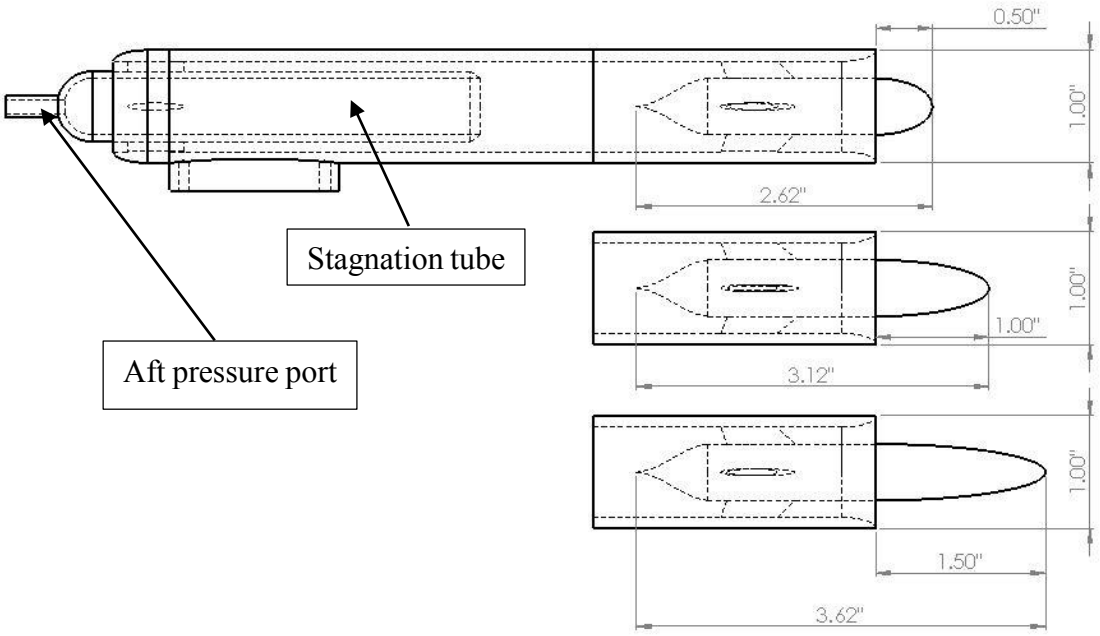

Figure 8: Bio-Inspired Probe Prototype with Different Centerbody Heads *(Top: L/D 0.5, Mid: L/D 1.0, Bottom L/D 1.5)*

4 Computational Fluid Dynamics Simulations and Set-Up

The computational fluid dynamic analysis would focus on the prototype novel probe with protruding centerbody of L/D 1.5. Theoretically, the novel probe with larger protruding centerbody of L/D 1.5 would have a better flow sensitivity over L/D 0.5 and 1.0. Since L/D 1.5 has a larger protruding centerbody, flow capture area is bigger. This chapter will discuss the computational simulation performed on the Bio-Inspired probe using CD-Adapco STAR-CCM+ CFD solver.

4.1 STAR-CCM+

STAR-CCM+ is a comprehensive engineering physic solver developed by CD-Adapco. The CFD software featured meshing of computational domain, automatic surface repair, surface wrapper, in built CAD modeling, solid and fluid flow simulation, as well as turbulence modeling. Along with is quick and easy user support, STAR-CCM+ is a user friendly software great for newcomers to CFD simulations. Further details on STAR CCM+ can be found on CD-Adapco's website[21].

4.2 Domain

The domain of the simulation model is constructed according to the dimension of the wind tunnel test section. Since the Bio-Inspired probe is an asymmetrical probe, symmetry profile as shown on Figure 9, is used to reduce the size of domain, shortening execution time for the simulation. Figure 10, illustrate the dimension of the simulation domain.

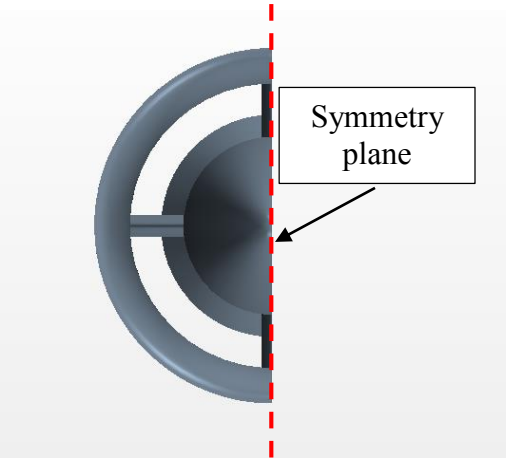

Figure 9: Front view of probe with symmetry plane

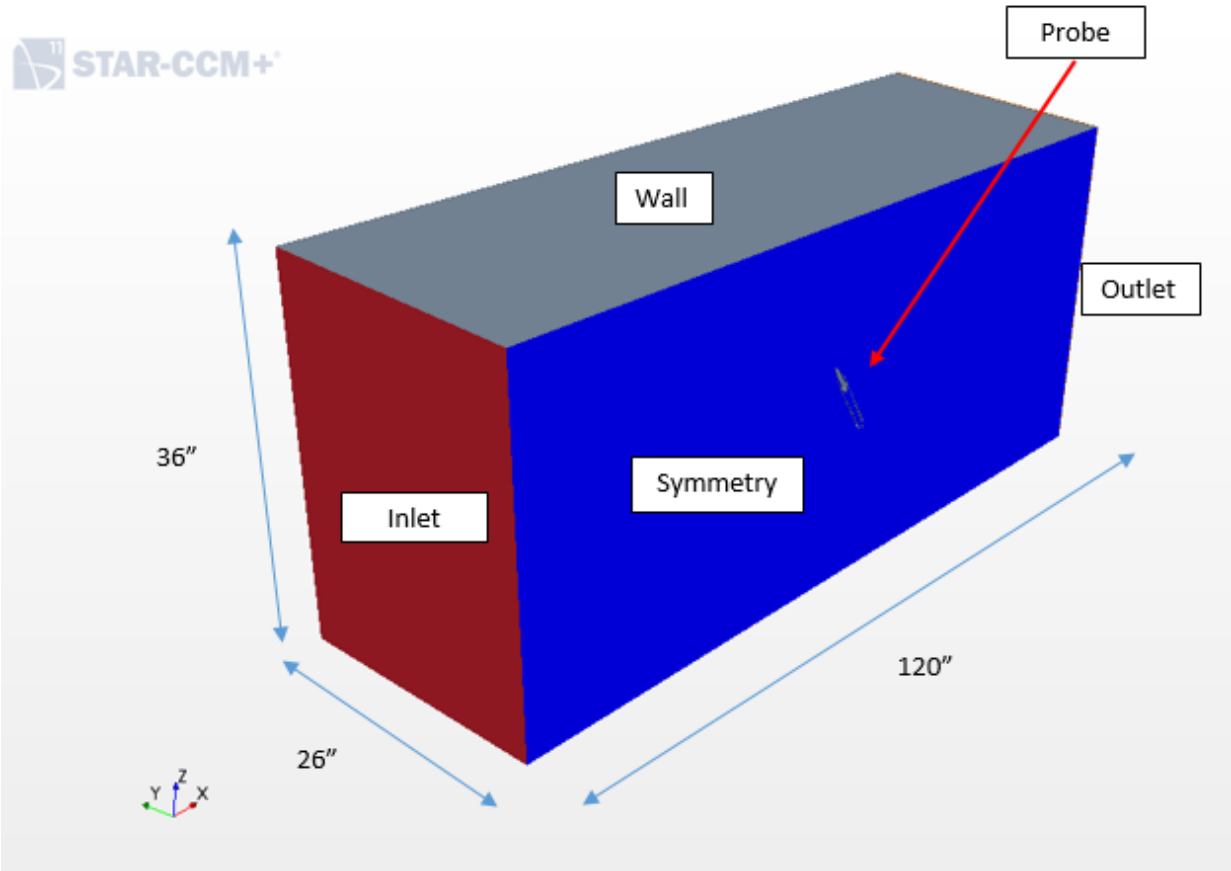

Figure 10: STAR CCM+ domain geometry

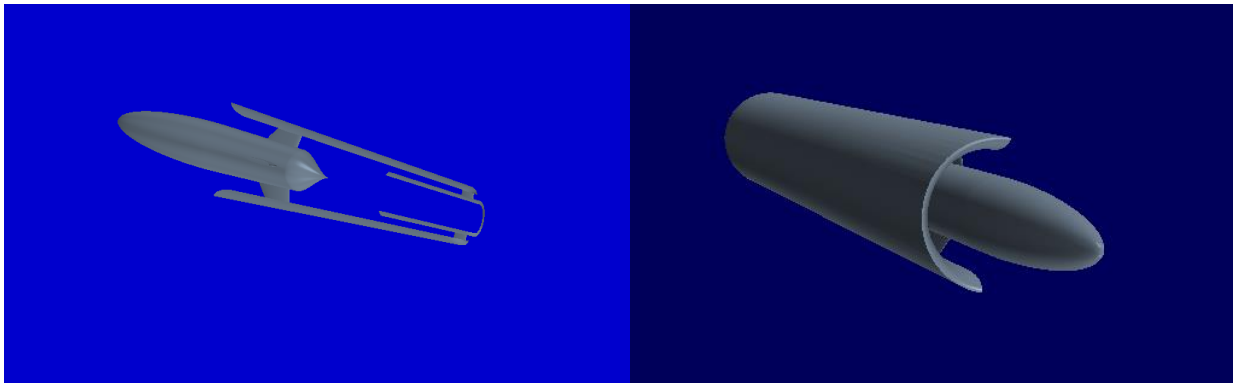

Figure 11: Probe on symmetry wall (zoom in)

4.3 Mesh

For meshing, unstructured regional-based 'mesh continua' method is used. Mesh continuum on STAR-CCM+ is a computational domain which mesh is created using a collection of surface meshing and volume meshing models. Surface cell size and volume growth rate is easily customizable. The topology and extent of the continuum can be defined by the input geometry created by the user[22].

Tetrahedral and polyhedral mesh are options for the mesh continua. Polyhedral mesh is selected for the simulation, since polyhedral mesh offers a significant accuracy benefits over the use of tetrahedral mesh at high angle of attack. Prism cells are added in the domain to account for boundary layers.

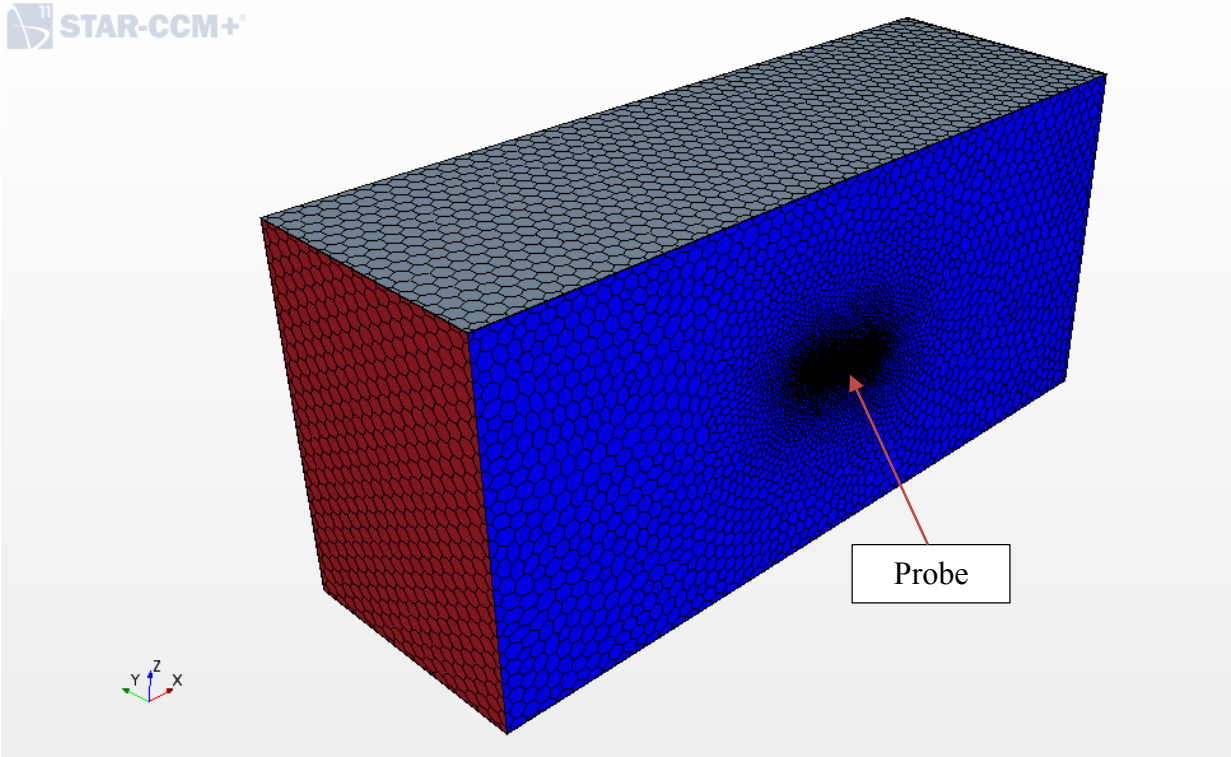

Figure 12: Domain with polyhedral mesh

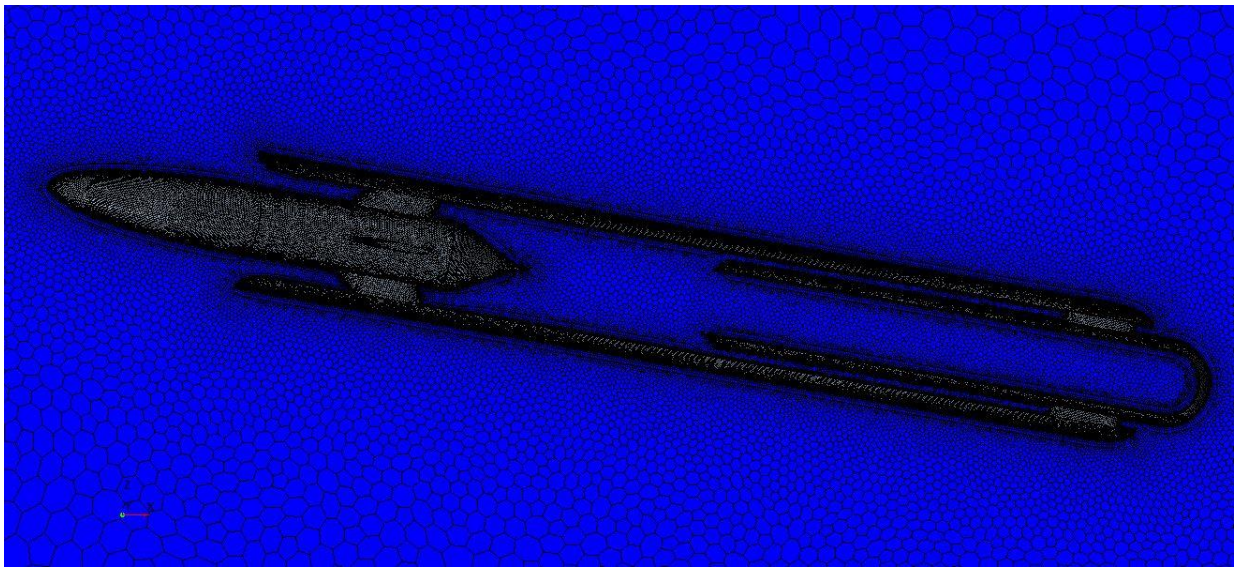

Figure 13: Bio-Inspired probe (L/D 1.5) with polyhedral mesh at 10°

In CFD analysis, validation is needed finalized the solution. Therefore it is important that simulation solution is independent of the discretized mesh used in the final solution. Typically, CFD analysis starts with a course mesh, solution is then iterated until all residuals reaches 10^{-3} or lower. A new mesh is refined by a factor of 2 and iterated again to convergence. If the calculated result of the refined mesh is within 5% of the result from the previous courser mesh, the mesh is assumed to be validated and independent from results. Cell size for the L/D 1.5 Bio-Inspired probe model were set at 0.016 inches for largest, and 0.00016 inches for smallest. The average total number of cells for the model is range at 2×10^6 to 3.5×10^6.

4.4 Physic Model

Novel probe L/D 1.5 will be simulated at inlet speed of 100 ft/s [30.5 m/s]. Physic model chosen to simulate the air flow over the Bio-Inspire probe include:

1. Steady flow
2. Ideal Gas Law
3. 3-D flow field

4. Segregated flow

Segregated flow solves flow equations (velocity and pressure) in a segregated and uncouple manner[23]. Since the simulation flow is steady, segregated flow is capable enough to provide accurate results with the benefit of less memory usage (faster yield).

Turbulence Model

Calculating Reynolds number (equation 4) is required to determine if flow is laminar or turbulent. The Bio-Inspire probe, yields a Reynolds number of 5.3 x 10^4. According to Holloway[16], flow over a cylinder body is at subcritical range ($300 < Re < 1.3 \times 10^5$), an early stage of transition phase. Flow would be laminar on the body and have a turbulent downstream after 80° from the leading edge of the protruding centerbody. Therefore, turbulent model would be used in the CFD analysis.

$$Re = \frac{\rho v D}{\mu} \qquad (1)$$

STAR-CCM+ comes with three basic turbulence modeling approaches, Reynolds Averaged Navier-Stokes (RANS) equations, Large eddy simulation (LES), and Detached eddy simulation (DES). According to literatures reviewed in chapter 2, using RANS equation models in this simulation is sufficient. Therefore the simulation conducted on the Bio-Inspired probe will utilized RANS equation models.

Due to the complex 3-D geometry present on the Bio-Inspired probe, it is not known which turbulent model will provide the best result. El-Behery[18] made comparison between eddy-viscosity turbulent models and Reynolds Transport model on an axisymmetric diffuser. His research concluded that Shear Stress Transport K-omega (SST k-ω) turbulent model and his own solver (derivative of the SST k-ω model) provided the most accurate results. To be certain that all best approaches are covered, the Bio-Inspired probe was tested with multiple turbulent

models. Four turbulent models available on STAR-CCM+ will be used in the simulation, which are:

1. Spallart-Allmaras (S-A)
2. K-Epsilon (k-ε)
3. Shear Stress Transport K-Omega (SST k-ω)
4. Reynolds Stress Transport (RST)

4.5 Reynolds Averaged Navier-Stokes (RANS) Turbulence Model

The RANS equations are directly resolved from the Navier-Stokes equations, where instantaneous velocity and pressure field are decomposed into a mean value and fluctuating components[22]. The averaging process is done with time averaging for steady-state situations and average of repeatable transient cases. The resulting mean equations would than appear as the original Navier-Stoke equation but with addition momentum transport equation (tensor quantity) included. The tensor quantity, T_t, known as Reynolds stress tensor, is define as:

$$T_t \equiv -\rho\overline{v'v'} = -\rho\begin{pmatrix} \overline{u'u'} & \overline{u'v'} & \overline{u'w} \\ \overline{u'v'} & \overline{v'v'} & \overline{v'w'} \\ \overline{u'w'} & \overline{v'w'} & \overline{w'w} \end{pmatrix} \qquad (2)$$

T_t can then be model in terms of mean flow quantities and provide closure to the governing equations. Two basic approaches are the eddy viscosity models and Reynolds stress transport models.

Eddy Viscosity Models

The concept of turbulent viscosity, μ_t is used in eddy viscosity models to model the stress tensor as function of mean flow quantities. The Boussinesq approximation which is the most common eddy viscosity model derives stress tensor as:

$$T_t = 2\mu_t S - \frac{2}{3}\left(\mu_t \nabla \bullet v + \rho k\right) I$$
$$S = \frac{1}{2}\left(\nabla v + \nabla v^T\right) \qquad (3)$$

S is the strain tensor and k is the turbulent kinetic energy. The Spalart-Allmaras, K-Epsilon and K-Omega are one- and two-equations eddy viscosity models. These models solves additional transport equation for scalar quantities of turbulent viscosity, μ_t, derivation. The two-equation models extend the linear approximation to include non-linear approximation, since Tt is linearly proportional to the mean strain rate and is known to be flawed[22].

Spallart-Allmaras (S-A)

A one transport equation model that determines turbulent viscosity. The S-A model is good for applications that has large attached boundary layers and mildly separated boundary layers. The S-A model is the simplest of all eddy viscosity models, therefore it has time efficiency benefit when compared to other RANS turbulent models

Realizable K Epsilon (*k-ε)*

Designed for circulation flow, k-ε is a two-equation model with compromise between robustness, accuracy and computational cost. The model solves transport equation for turbulent kinetic energy k and dissipation rate ε. Realizable approach contains a new transport equation for the turbulent dissipation rate, ε. In addition, critical coefficient, C_μ, is expressed as a function of

mean flow with influence from turbulence properties. The model in turn is better when compared to standard k-ε and able to produce better results[22].

Shear Stress Transport K-Omega (SST *k-ω*)

Similar to k-ε, k-ω model is a two transport equation with k being turbulent kinetic energy. The main difference when compared to k-ε is in the second transported turbulence variable quantity, ω. The SST model added additional non-conservative cross-diffusion term containing dot product of Δk and Δω. This addition was to address the standard k-ω model poor sensitivity to free-stream or inlet conditions.

Linear Pressure Strain Two-Layer-Reynolds Stress Transport (RST)

RST model are known as second-moment closure models which solves each component of the Reynolds stress tensor. It is complex and computationally expensive model. For example, simulation for Bio-Inspired probe at 0° angle running at 8 parallel cores and 16 GB RAM, SST *k-ω* model took about 480 minutes to reach convergence criterion at 10^{-3}, while RST model took 840 minutes to reach the same convergence criteria, about twice the computation time. The increase in computation time is due to the model having to solve seven equations with high iterations and numerical stiffness due to convergence criteria.

4.6 Results

Pressure

Bio-Inspire probe L/D 1.5 is simulated at flow angle, θ, range from 0° to 60°, at inlet speed of 100 ft/s. The probe was simulated with four turbulent models, S-A, k-ε, SST k-ω and RST and the dynamic pressure contour on the probe was recorded.

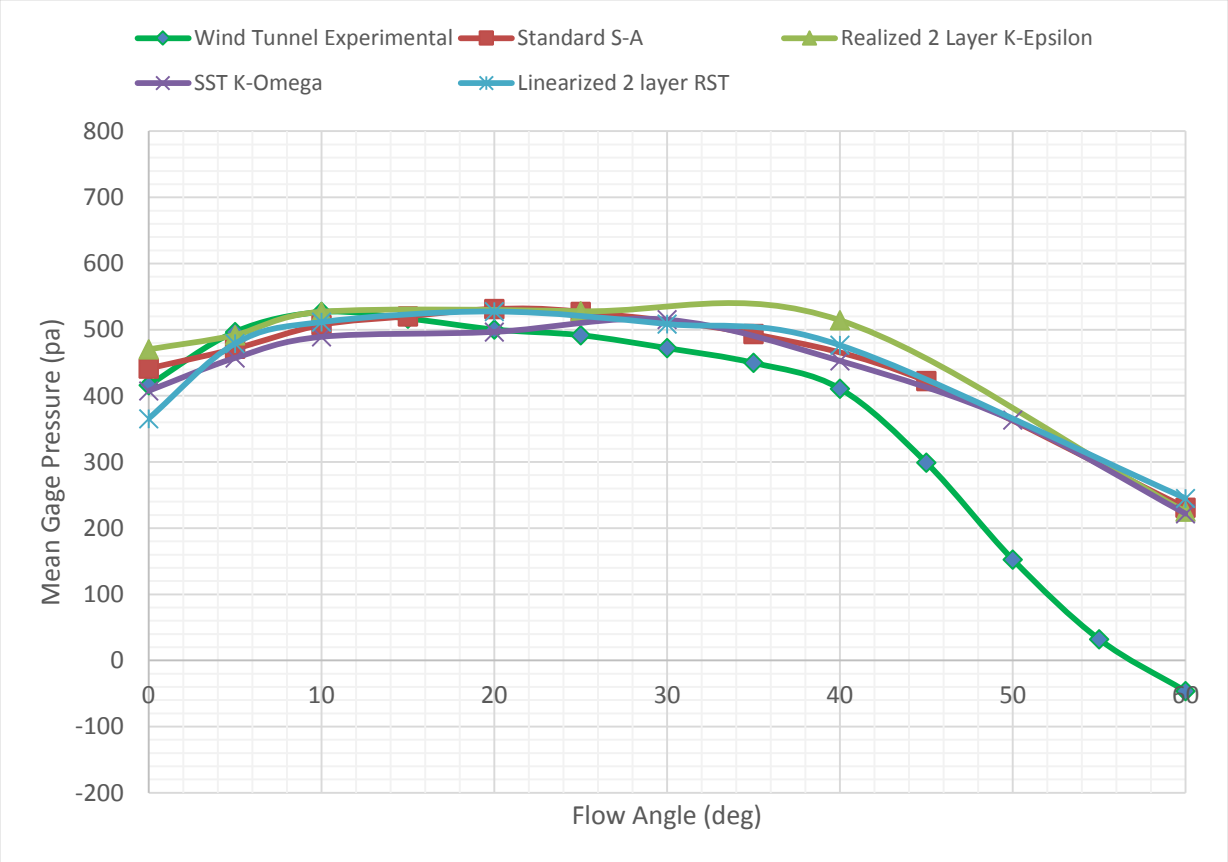

Figure 14: CFD turbulent models dynamic pressure measurement at flow angularity at 100 ft/s, [L/D 1.5 Probe]

Experimental data from preliminary wind tunnel test at 100 ft/s with L/D 1.5 head was compared with the dynamic pressure at aft stagnation tube from all four turbulent models on Figure 16. All turbulent models have similar dynamic pressure measurement trend at θ = 0° to 60°. The dynamic pressure contours are shown from Figure 15 to Figure 18.

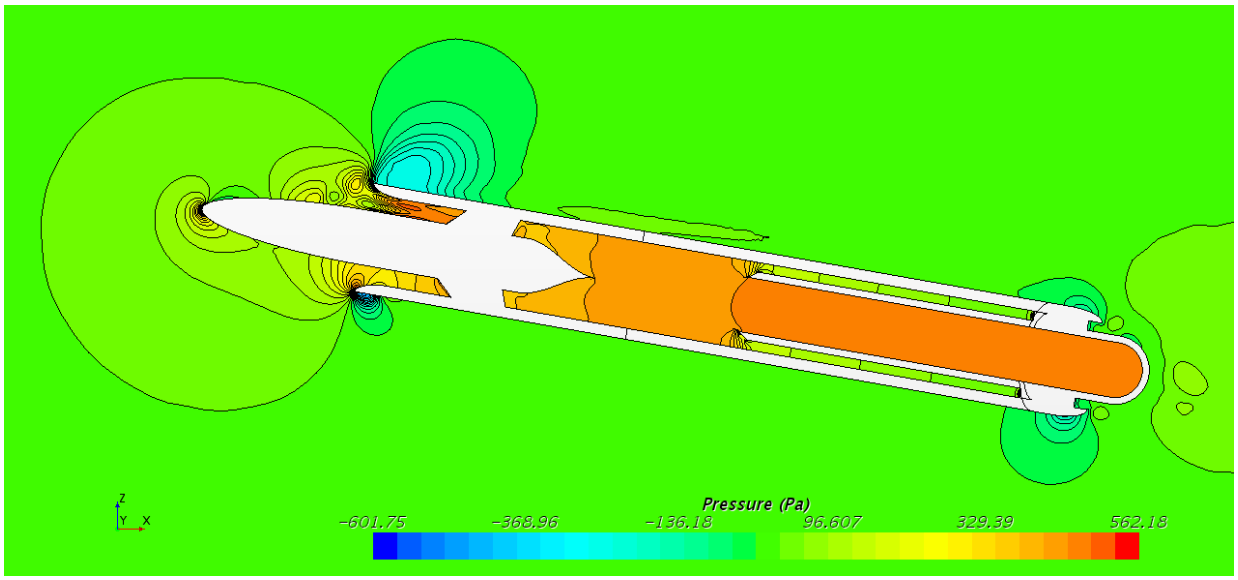

Figure 15: Differential pressure value across probe at 10° flow angle [S-A model]

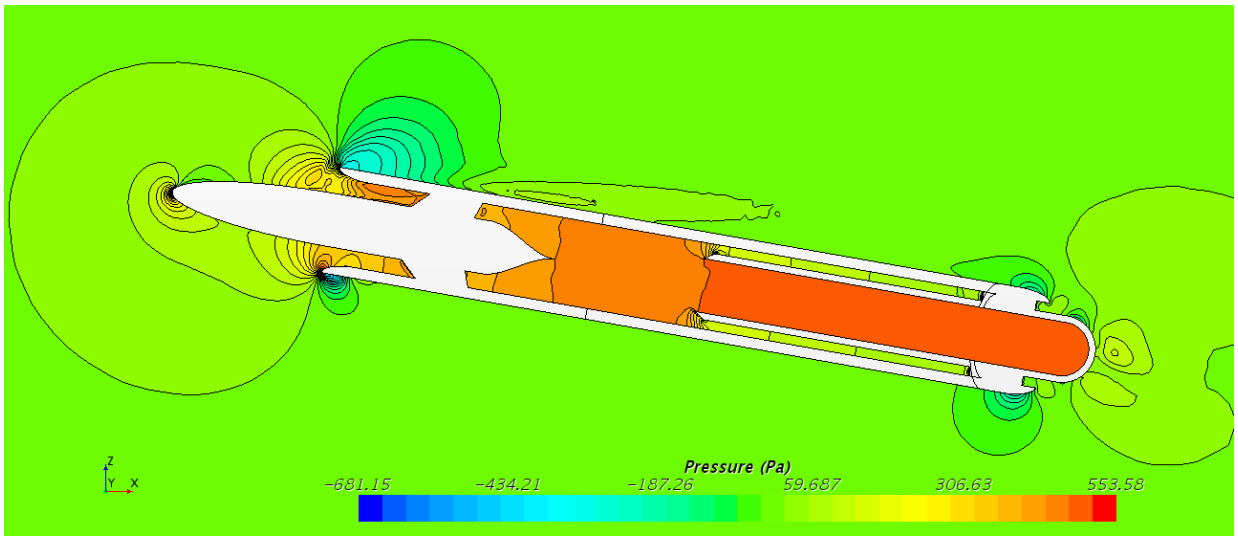

Figure 16: Differential pressure value across probe at 10° flow angle [*k-ε* model]

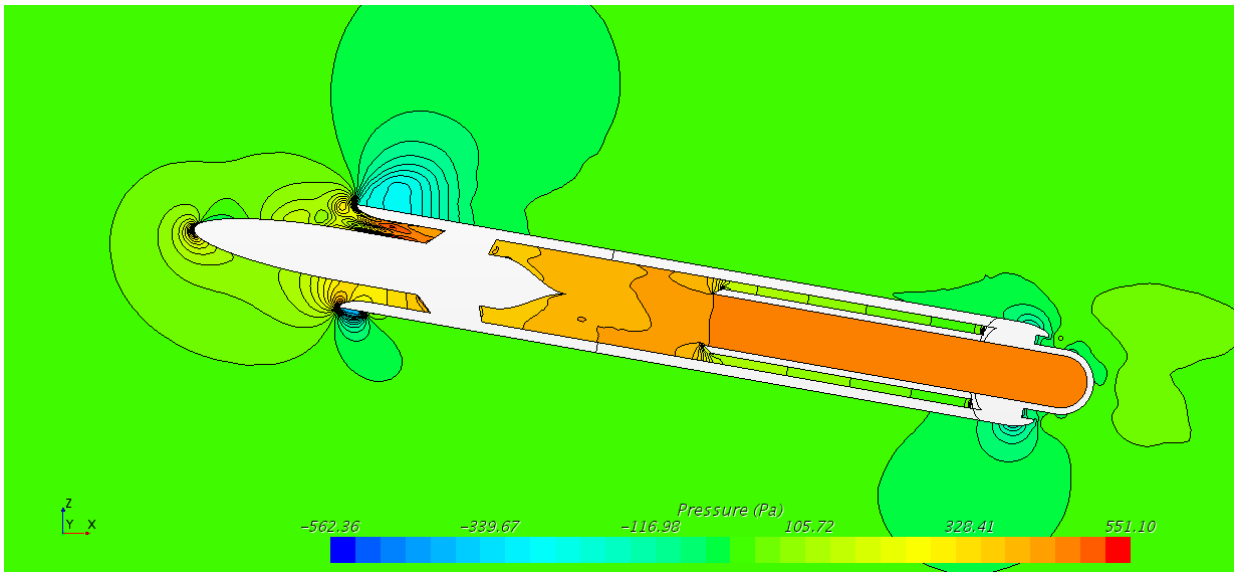

Figure 17: Differential pressure value across probe at 10° flow angle [SST *k-ω* model]

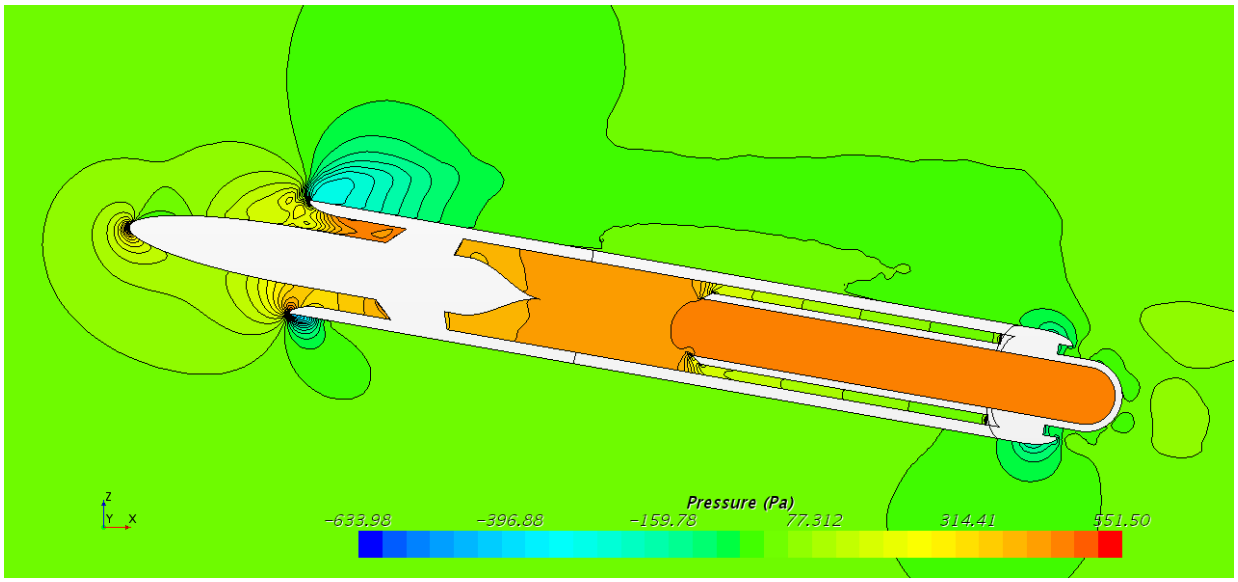

Figure 18: Differential pressure value across probe at 10° flow angle [RST model]

A key difference between computation and experimental results is the deviation of dynamic pressure measurement from flow angle 40° to 60°. Figure 16 showed that computational simulation of all 4 turbulence models have a smaller dynamic pressure loss rate when compared to preliminary experimental results. Surprisingly, RST also deviated at $\theta > 40°$. It is likely the physic models fails to predict flow separation and swirl in the probe as mention in the literature

review[19]. For validation, an additional simulation is conducted on a geometry of a conventional Pitot-static. Similar physic models and initial conditions were used. As no difference between the turbulent models is found when calculating dynamic pressure, only SST k-ω is used instead. The computational result and preliminary wind tunnel results of a conventional pitot-static tube are compared to the experimental results on Figure 19.

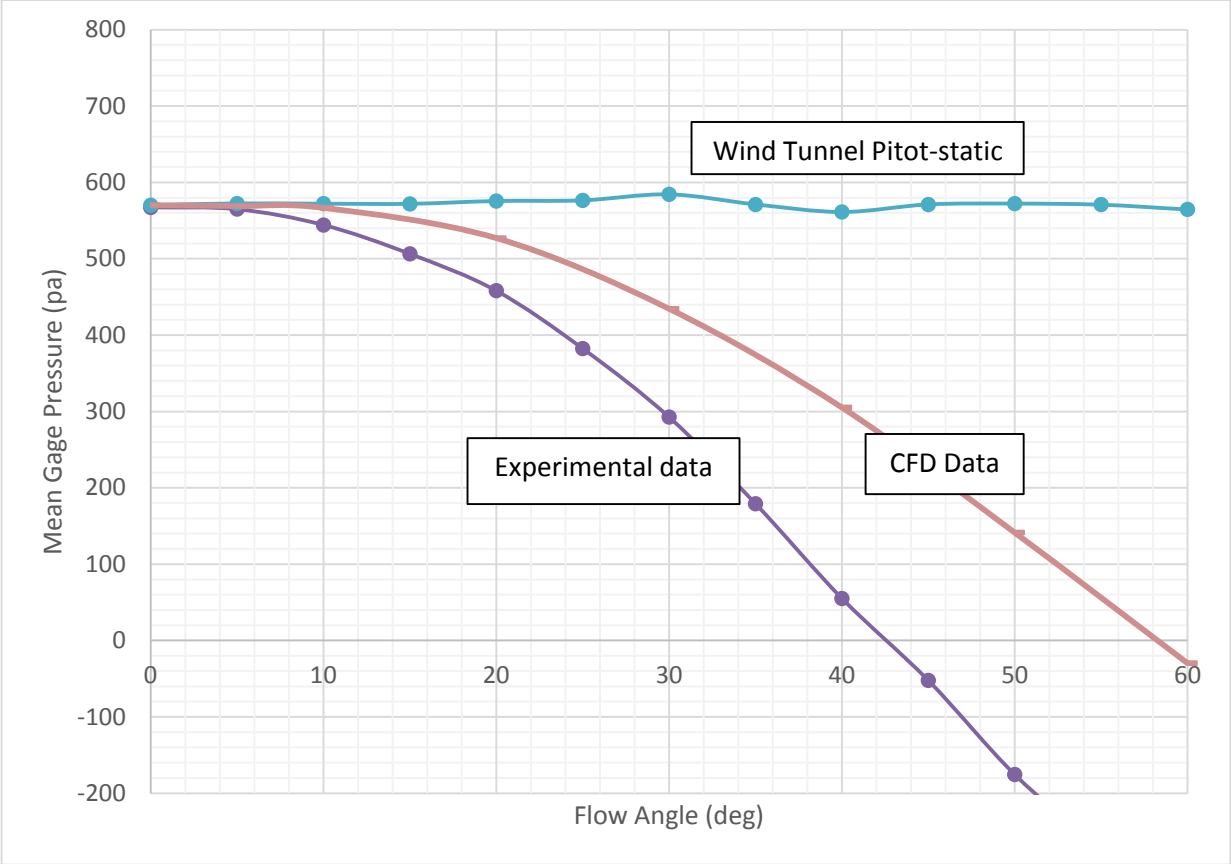

Figure 19: Conventional Pitot-static conventional pressure measurement

According to Figure 23, CFD results has a lower pressure drop rate compare to experimental data. The slower pressure drop indicates slower flow separation than wind tunnel experimental results. According to both Figure 15 and 18, it is concluded that the embedded RANS equation turbulent models provided by STAR-CCM+ is not capable of simulating accurate results at high angle of attack with the presence of high flow separation and swirl. To

achieve accurate data on complex 3D geometry with swirl involved, solvers have to be designed to account for vorticity and swirling effects. This problem was explained in a case study done by Cheng and Farokhi[19]. The embedded turbulent models is designed and optimized for flow separation on flat plate or simpler geometries. A case study done by Halloway[16], reported that standard one- and two-equation turbulent model could not accurately account for flow separation on a cylindrical body. Changes are needed on the turbulent models to reduce simulation errors.

Streamline Flow

In the case on how flow acts on the Bio-Inspired probe's protruding centerbody, streamlines were visualized on STAR-CCM+ as seen on Figure 20 to Figure 23. The following figures illustrate streamline across the Bio-Inspired probe L/D 1.5 at inlet speed of 100 ft/s on all four turbulent models.

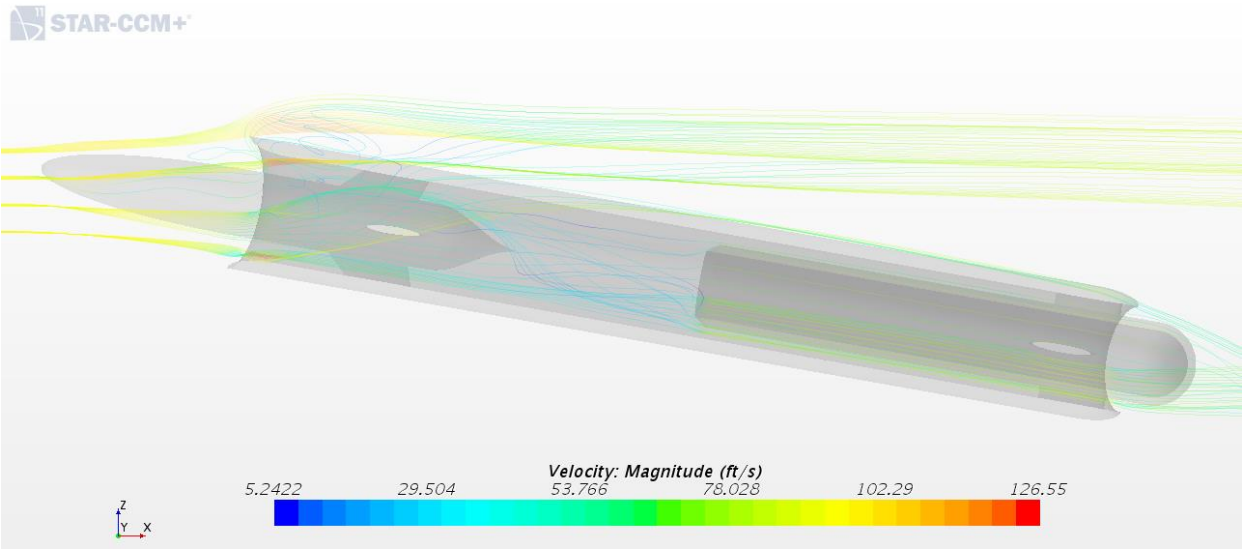

Figure 20: Streamline on probe (L/D 1.5) at 100 ft/s, θ= 10° [S-A model]

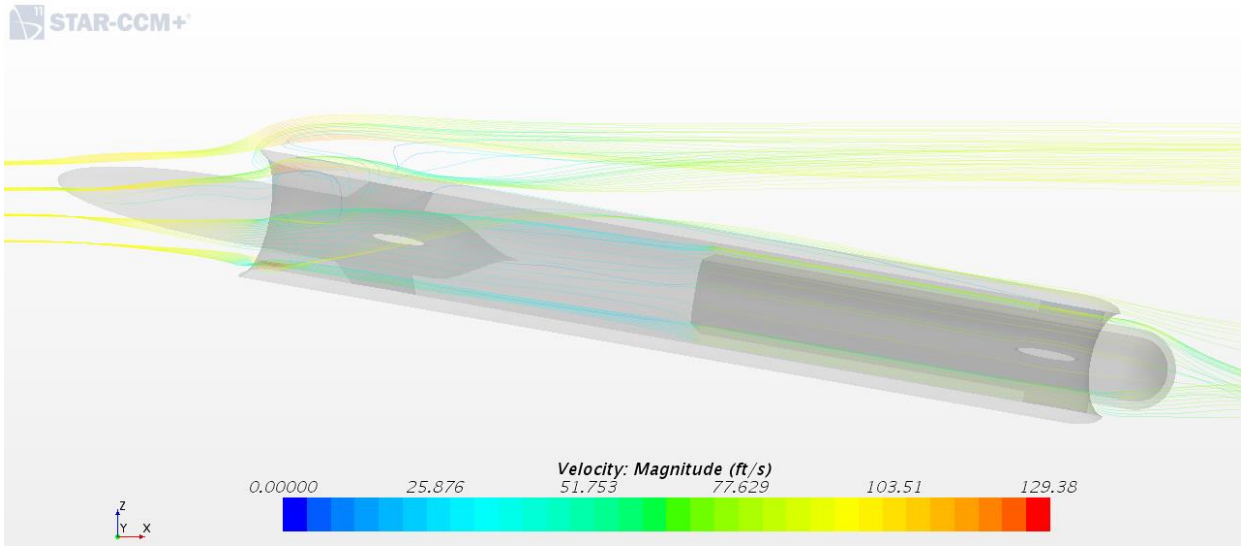

Figure 21: Streamline on probe (L/D 1.5) at 100 ft/s, θ= 10° [*K-ε* model]

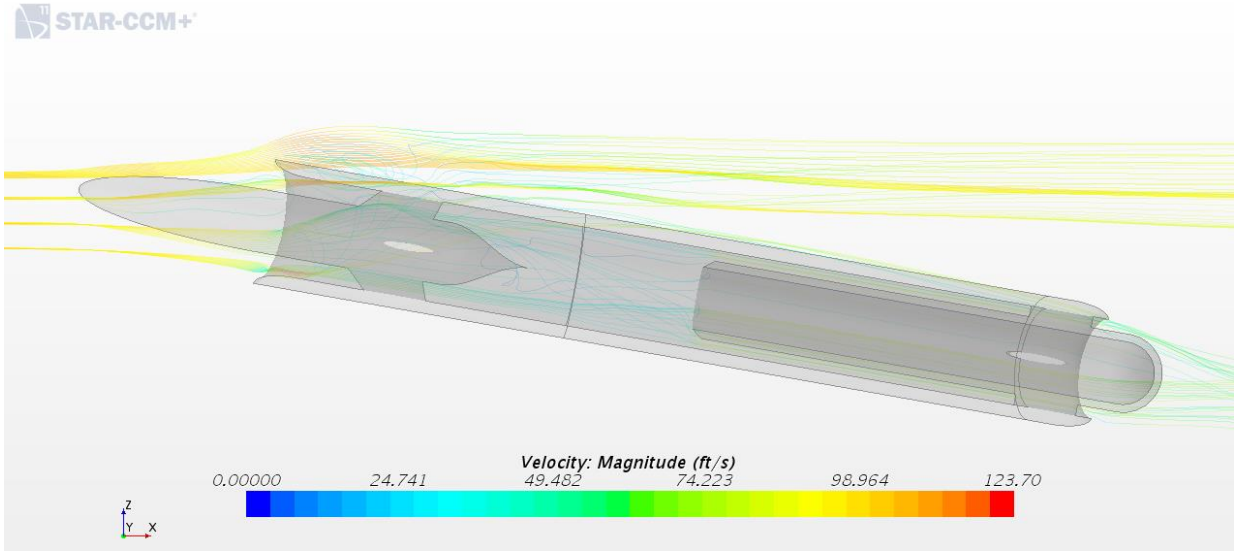

Figure 22: Streamline on probe (L/D 1.5) at 100 ft/s, θ= 10° [SST *K-ω* model]

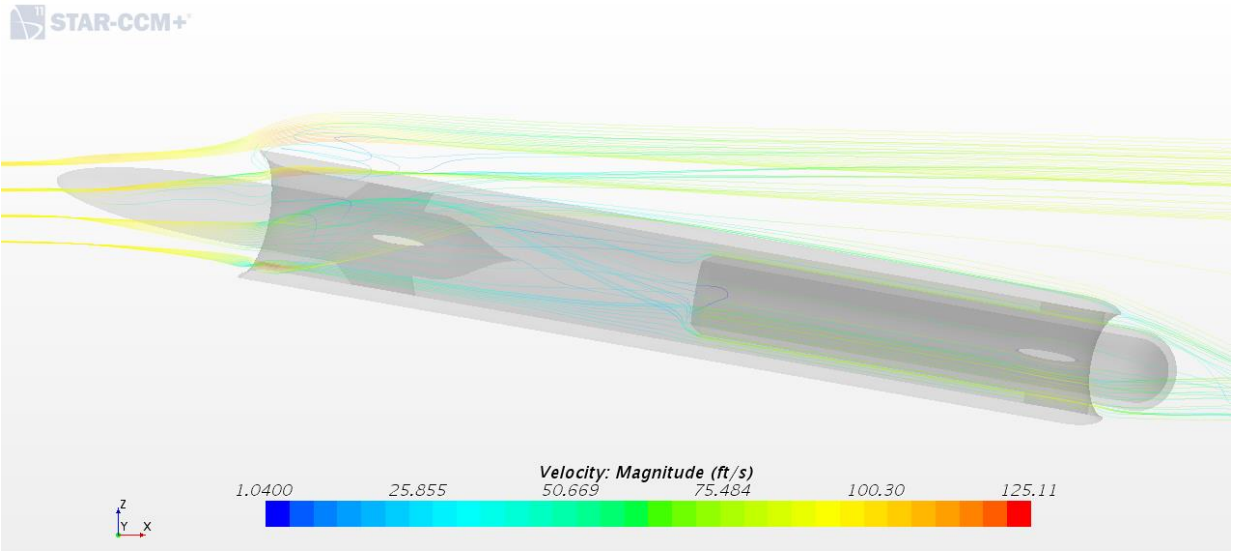

Figure 23: Streamline on probe (L/D 1.5) at 100 ft/s, θ= 10° [RST model]

Besides the difference in streamlines in the wake region aft of the protruding centerbody, all four turbulent models clearly have streamlines that are attached on the probe's protruding centerbody. The results validates the ability of the probe's centerbody to capture flow through the use of Coanda effect. The existence of an aft vent enable throughflow through the probe, making flow attachment on protruding centerbody possible. The spiral rotation of the flow on the protruding centerbody is due to the vorticity cause of by the inlet geometry of the Bio-Inspired probe's inlet. Shear stress on the centerbody, Figure 24, also illustrate the flow spiral attachment on the centerbody. Flow continues to attach to the centerbody up to θ = 60°, seen on Figure 26, evident on the flow existing out of the aft vent of the probe.

Shear Stress

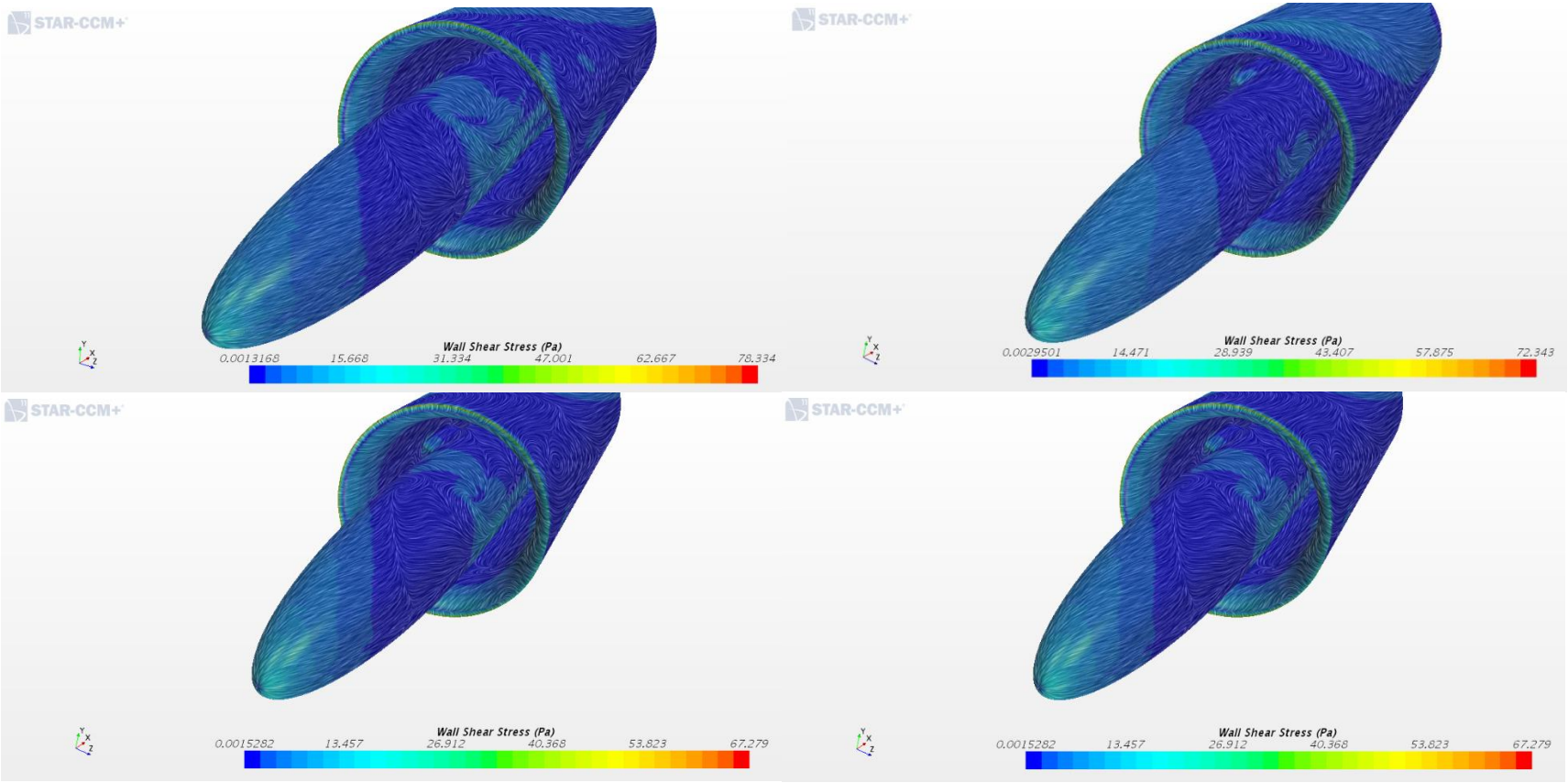

Figure 24: Skin shear stress on centerbody [top left: S-A, top right: k-ε, bottom left: SST k-ω, bottom right: RST] (Inlet speed 100 ft/s)

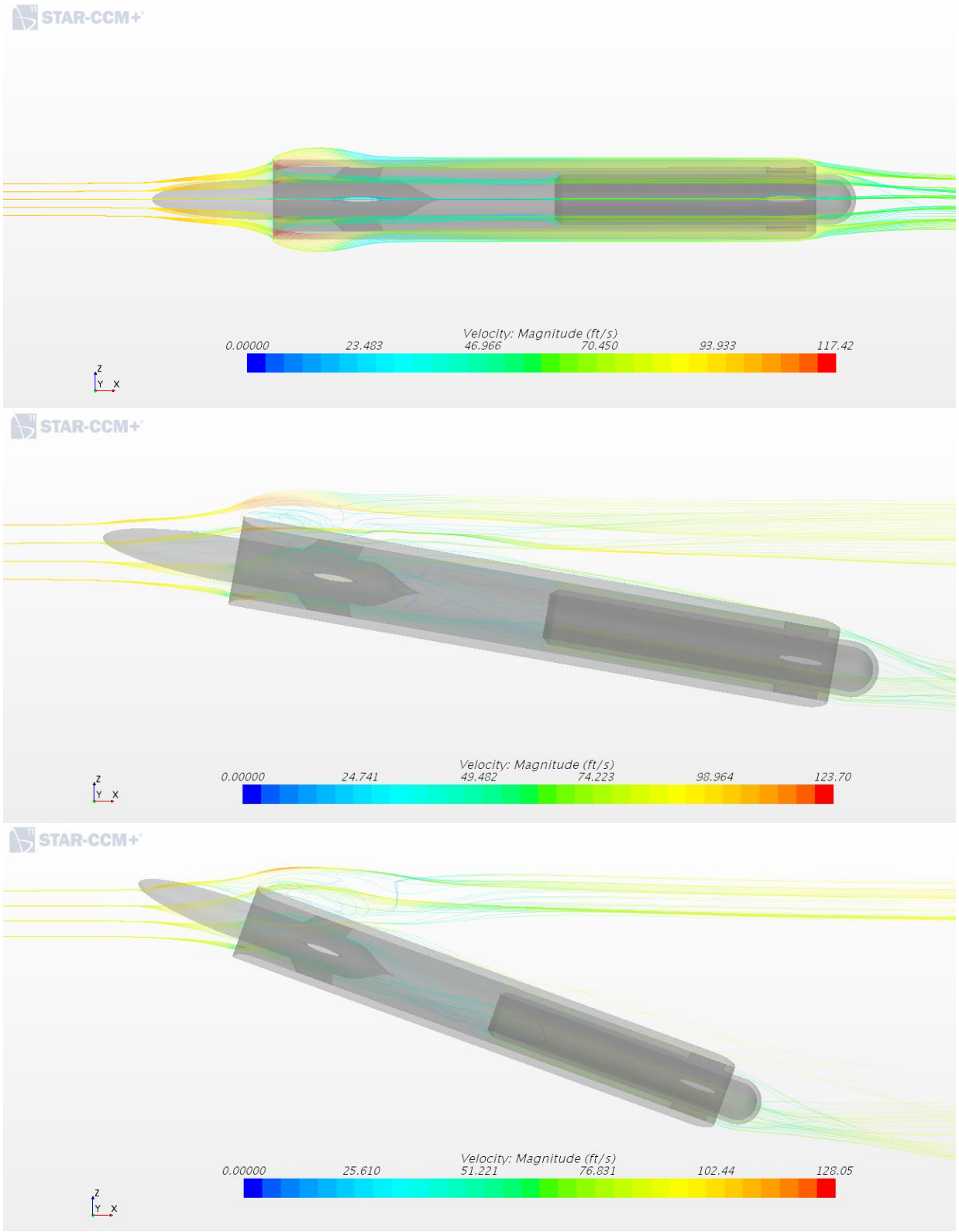

Figure 25: Streamlines across Bio-Inspired probe L/D 1.5 at θ = 0°, 10°, 20° [SST k-ω]

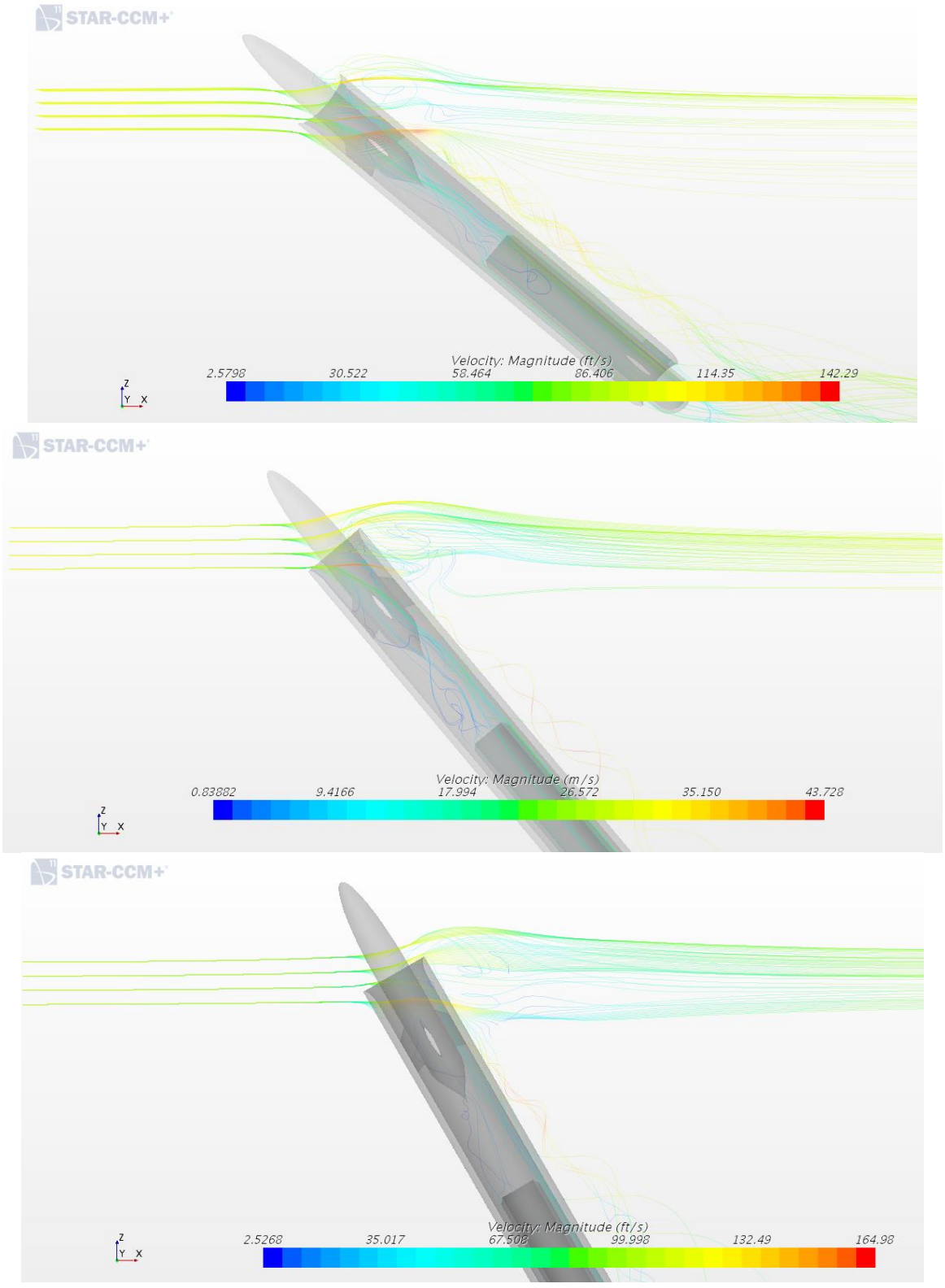

Figure 26: Streamlines across Bio-Inspired probe L/D 1.5 at θ = 40°, 50°, 60° [SST k-ω]

5 Wind Tunnel Experiment

The goal of the wind tunnel experiment is to investigate the angular sensitivity of the Bio-Inspired probe. Three novel airspeed probes with different protruding centerbody heads (L/D 0.5, 1.0 and 1.5) and a single conventional Pitot-static probe will be tested. Total pressure is then measured on the aft module of the Bio-Inspired probe at three speeds of V = 90 ft/s, 100 ft/s and 115 ft/s. The test was conducted between flow angles, θ = 0° and +60° with a +5° degree increment. Wind tunnel data acquisition and data processing is performed by the used of LabView and MATLAB. This chapter will include description on probe calibration, wind tunnel set-up and wind tunnel experiment results.

5.1 Probe Calibration and Pressure Measurement

During the wind tunnel test, total pressure, P_t, will be measured at the aft pressure port as seen on Figure 2. Since the pressure sensor in the Bio-Inspired probe's stagnation tube is located downstream of the centerbody, total pressure, P_{t0}', measured would not be equal, but less when compared to the freestream total pressure, P_{t0}. The centerbody drag, $(\Delta p_t)_{C_D}$, primarily contributes to the pressure loss on P_{t0}'. Thus the calibration correction is define as:

$$p_{t0} = p'_{t0} + (\Delta p_t)_{C_D} \tag{4}$$

The total pressure loss, ΔP_t, in equation 4 is measured in a wind tunnel test using a side-by-side configuration tunnel test of a Bio-Inspired probe and an alpha beta vane swirling head pitot static probe. This calibration of pressure correction is shown on Figure 27. However, due to flow angularity present in this experiment, equation 4 is required to resolve further into equation 5 to account for additional drag gain at $\theta \neq 0$.

$$(\Delta p_t)_{C_D} = (\Delta p_t)_{C_{D0}} + \delta \left| (\Delta p_t)_{C_{D0}} \right|_{\theta \neq 0} \tag{5}$$

The first term, $(\Delta p_t)_{C_{D0}}$, is total pressure loss at θ = 0. Second term, $\delta[(\Delta p_t)_{C_{D0}}]_{\theta\neq 0}$, is the increment in drag due to centerbody lift and side force at flow angles other than zero. Although the baseline friction and pressure drag, C_{D0}, is the main source to the pressure loss. Lift and side force from the aerodynamic shape of the centerbody and slender streamline bodies of revolution still contribute to centerbody drag, but drag is the primary contributor. Correction due to centerbody drag can be further resolved into first-order and second-order under perturbation terms:

$$\begin{aligned} p_{t0} &= p_{t0}^{'} + \left(\Delta p_t\right)_{C_D} \\ &= p_{t0}^{'}\left\{1 + \frac{\left[\left(\Delta p_t\right)_{C_{D0}}\right]_{\theta=0}}{p_{t0}^{'}} + \frac{\delta\left[\left(\Delta p_t\right)_{C_{D0}}\right]_{\theta\neq 0}}{p_{t0}^{'}}\right\} \\ &= p_{t0}^{'}\left[1 + 0\left(\varepsilon\right) + 0\left(\varepsilon^2\right)\right] \end{aligned} \qquad (6)$$

For this wind tunnel test experiment, only total pressure loss correction due to C_{D0}, can be applied to the Bio-Inspired probe at zero flow angularity. A new measuring device is needed to measure drag at θ ≠ 0, which is beyond the scope of this project. Thus total pressure calibration is only corrected to total pressure loss at 0 degree flow angle.

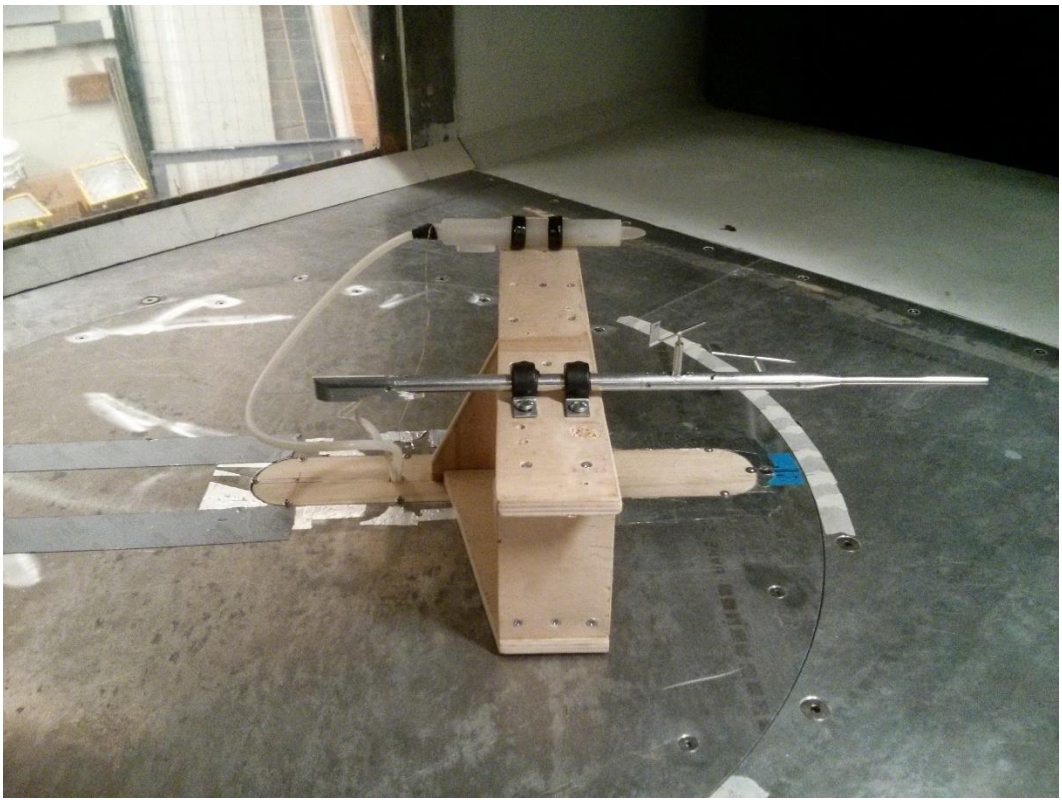

Figure 27: Bio-Inspire probe calibration on custom stand along with alpha-beta vane pitot static probe

5.2 Wind Tunnel Set-up

Wind Tunnel

University of Kansas featured a close loop (recirculating) horizontal low speed wind tunnel with two test section chambers. The test section used in this experiment is the upper smaller test section with dimension: 51 inch wide, 36 inch high and length of 60 inches. The wind tunnel is powered by a 300 HP electric motor with a 4 bladed variable pitch control propeller capable generating wind speed of 0 to 200 mph at the test section. The tunnel has a contraction ratio of 9:1 and turbulence factor of 1.1 at 140 mph. The test section is equipped with a 6-component pyramid balance and a flat rotating turntable.

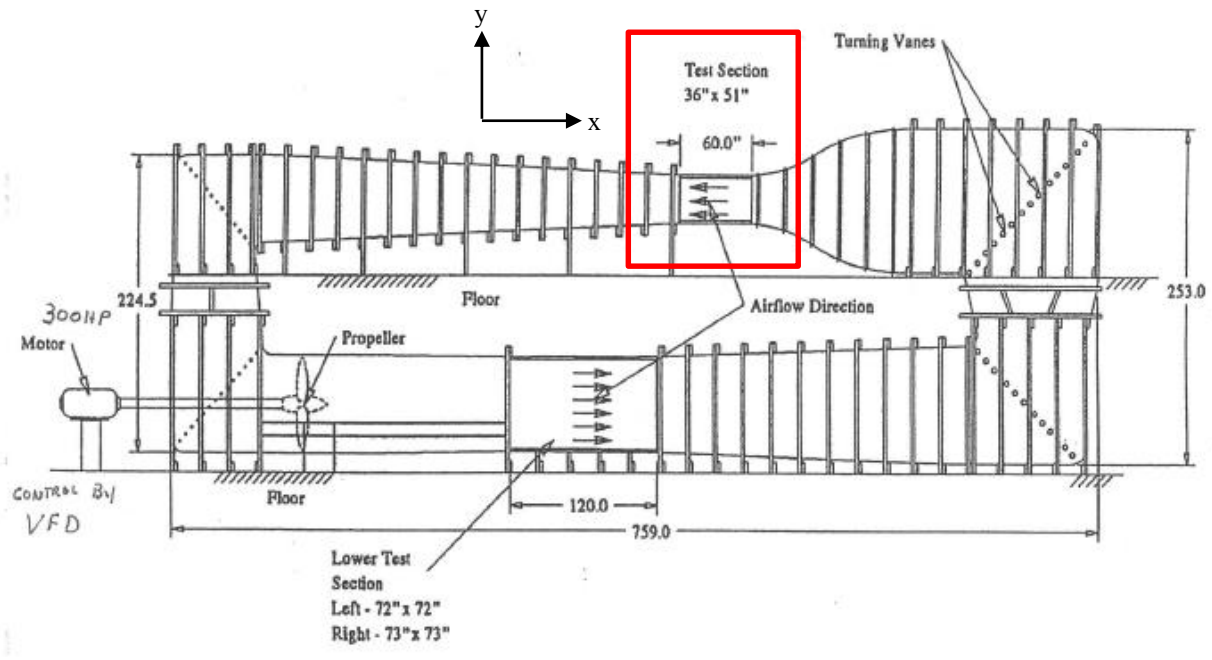

Figure 28: University of Kansas low speed wind tunnel layout [test section used in red]

Figure 29: Wind tunnel test section

A Pitot-static tube located in the test section measures the dynamic pressures and through the use of Bernoulli's in equation 9, test section wind speed is calculated and output on DAQ. The wind tunnel is also equipped with a 2 of static ports use to validate test section wind speed. They are located in the test section and in the upwind chamber of the test section.

Figure 30: Wind tunnel Pitot-static tube (left) static port (right)

Probe Set-up

The 3 Bio-Inspired probes (L/D 0.5, 1.0, and 1.5) and a conventional Pitot-static tube are installed side by side along a vertical flat plate stand bolted on a horizontal rotating table in the test section as seen on Figure 27. The stand was turned in increment of 5° with respect to y-axis (sideslip, β) of the test section. Since the probe is axisymmetric, sideslip can be assumed as angle of attack, α. The probes are set-up in the following order, shown on Figure 32, from the bottom of stand upwards: conventional Pitot-static, L/D 0.5, L/D 1.5, L/D 1.0. A laser is used to align the installed probes to ensure they are parallel.

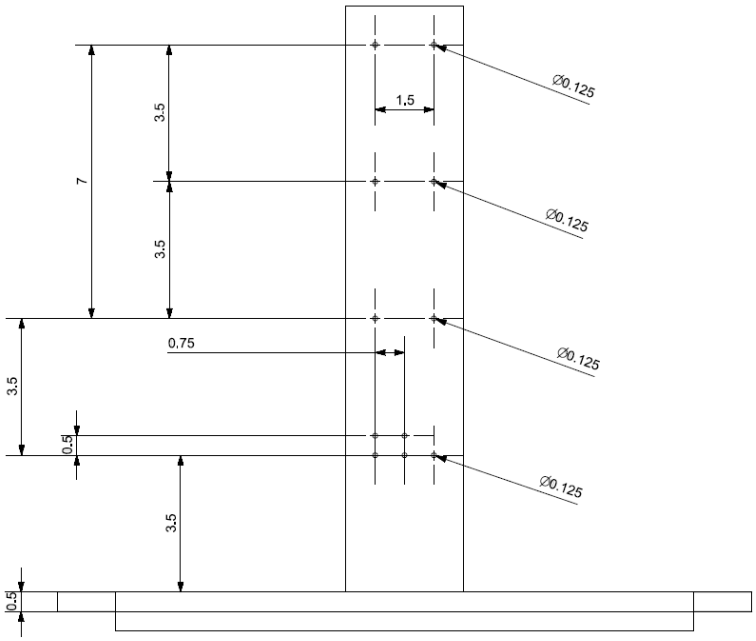

Figure 31: Vertical test stand dimension -*side view* (measurements in inches)

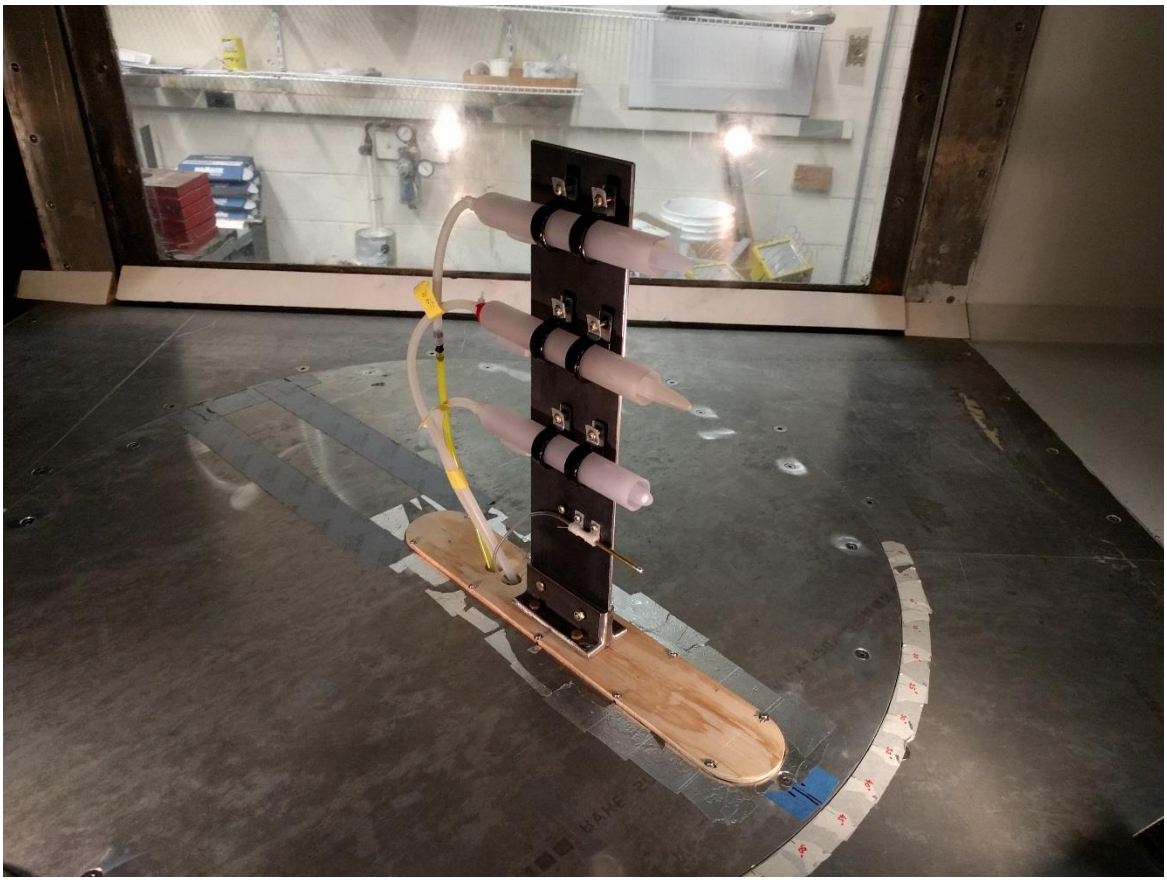

Figure 32: Probe set-up in wind tunnel test section

5.3 Data Acquisition

The probes are each equipped with an AMS 5812-0001-D, Figure 33, which is high a sensitive ultra-low differential pressure sensor. It comes with an analog and digital output (I^2C) and capable of differential or relative pressure measurement with a pressure range of 0-0.15 psi (0 – 10.34 mbar). It has an analog voltage range of 0.5-4.5V, at 4V of full span output (FSO). The AMS 5812 pressure sensor has an accuracy of ±1.5% FSO and overall error of ±2% FSO at temperature of -25 to 85°C.

Figure 33: AMS 5812 Pressure Sensor

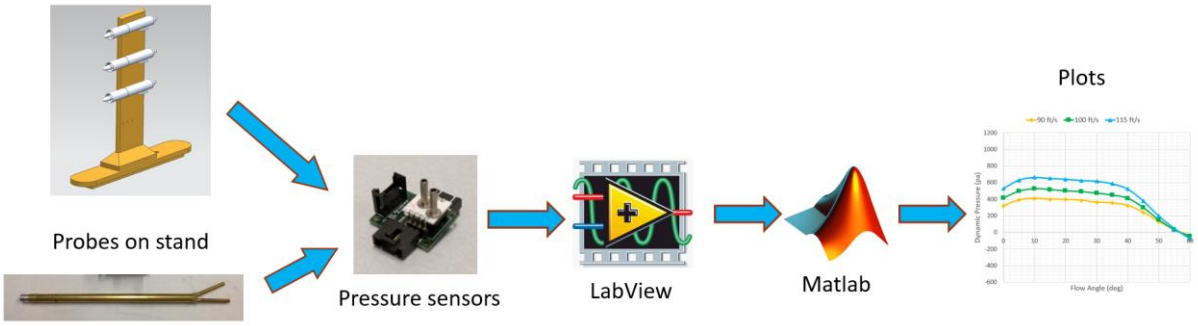

Figure 34: DAQ Process

Pressure Measurement and Data processing

Total pressure, P_t, is measured at the aft tube of all three Bio-Inspired probe. Static pressure, P_0 is the local pressure measured in the wind tunnel test section with the use of static ports in the test section, Figure 30. Both total pressure and static pressure are then fed into the differential pressure sensor, which in turn will output dynamic pressure, $\bar{q}$. Air velocity, V can be calculated from equation 9, decomposed from Bernoulli's equation, equation 7 and 8.

$$P_0 + \frac{1}{2}\rho V^2 = P_t \quad (7)$$

$$P_t - P_0 = \frac{1}{2}\rho V^2 = \bar{q} \quad (8)$$

$$V = \sqrt{\frac{2(P_t - P_0)}{\rho}} \quad (9)$$

Time resolved total pressure and static pressure measurements are collected at 1000 HZ. 20 sets of measurements are acquired at 30 seconds interval each. Statistical method of 95 percentile and Chauvenet's Criterion were applied on the data. All total pressure measurement are gage pressure with reference to ambient pressure. Test section temperature are at standard room temperature and density is consistently recorded at an average of 0.00223 slugs/ft^3.

Figure 35: Wind tunnel data acquisition

5.4 Wind Tunnel Results

Initial tests were carried out in range of ±60° to ascertain ±θ symmetry in flow measurement. Subsequent test are conducted from 0° < θ < 60° with 5° increment at 100 ft/s (30.5 m/s). Additional testing were performed with similar θ at wind speed of 90 ft/s (27.5 m/s), and 115 ft/s (35 m/s). Each result graph presents mean total pressure or mean dynamic pressure measurements measured from 5 probes in the wind tunnel, which are: 3 Bio-Inspired probes (L/D 0.5, 1.0, 1.5), and conventional Pitot-static tube side-by-side with Bio-Inspired probes. The wind tunnel Pitot static tube is always set at θ = 0°, therefore it will always record correct pressure measurement at variable θ.

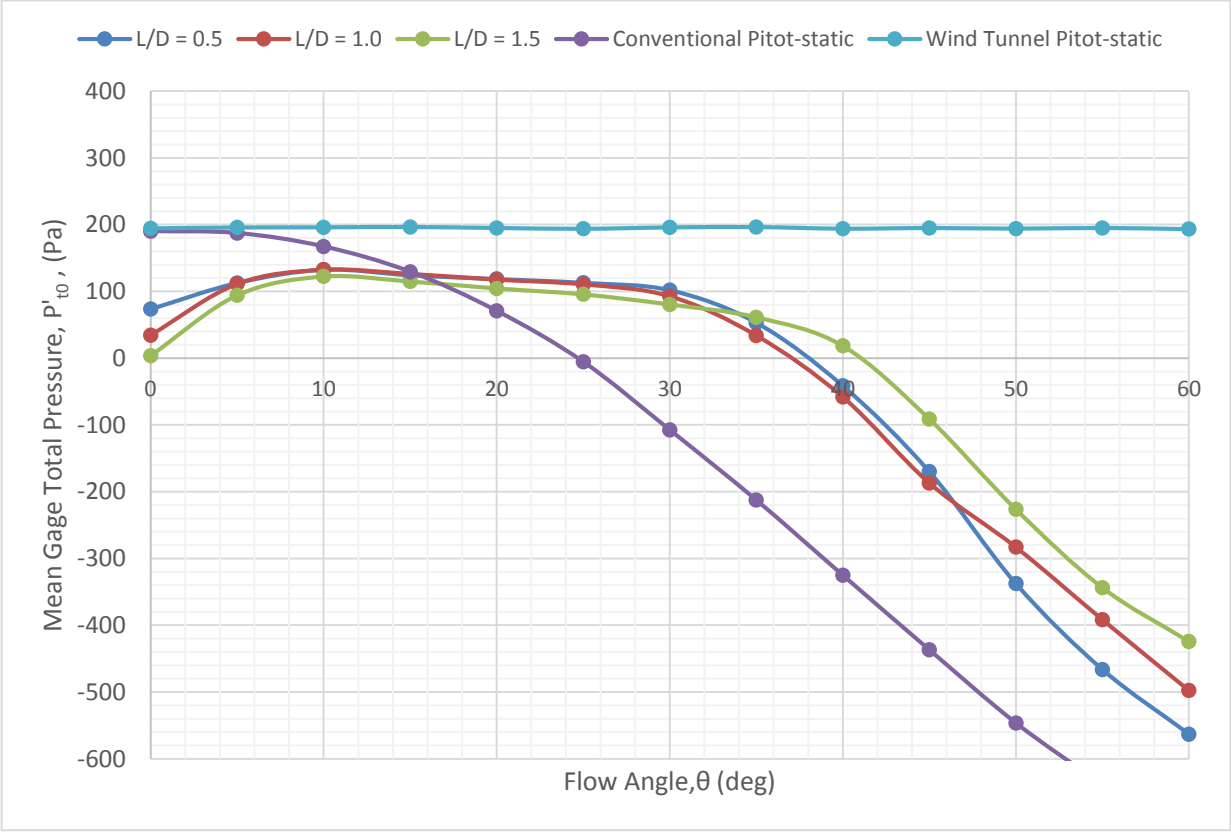

Figure 36: Uncalibrated mean total pressure at flow angularity of 4 probes [test section speed of 100 ft/s]

Wind tunnel pitot-static maintains a flow angle, θ of 0°, to provide constant total pressure readings when the Bio-Inspired probes and conventional Pitot-static are rotated to a specific flow angle. Bio-Inspired mean gage total pressure reading across the flow angles shown on Figure 36 (reference to room ambient pressure), are not calibrated to account for total pressure loss, $(\Delta P_t)_{Cd}$, due to centerbody drag. Although, total pressure readings of all three Bio-Inspired probe at 5° to 30° are constant, deviates 80Pa-100Pa off from the correct total pressure readings. Dynamic pressure in Figure 37, is reference to wind tunnel test section's static pressure.

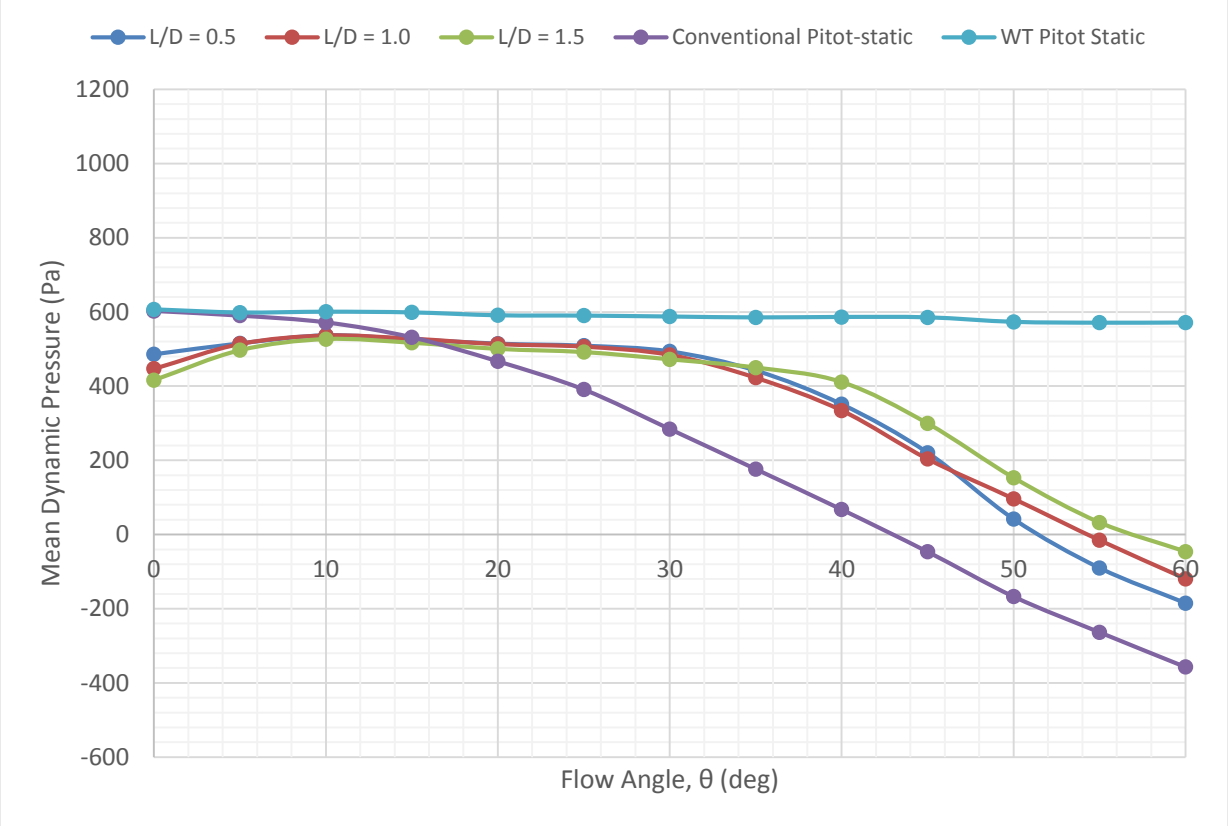

Figure 37: Uncalibrated mean dynamic pressure at flow angularity of 4 probes [test section speed of 100 ft/s]

Observing Figure 36 and Figure 37, all 3 Bio-Inspired probe at θ = 0°, suffers total pressure loss of 50 Pa to 120 Pa due to drag. Total pressure measurements were quickly recovered

when flow angle increases and leveled off at $\theta = 10°$. Total pressure measurements would remain almost constant from flow angle of 10° to 30°, with only a small total pressure loss rate of ≈ 2.5 Pa/deg. Due to centerbody drag, Total pressure measurement would still be offset by 100 Pa between the Bio Inspired probe and the correct total pressure and dynamic pressure measurements output by the wind tunnel Pitot-static. These pressure offset is calibrated in Figure 38, where pressure loss at $\theta = 0°$ is added back to the mean dynamic pressure value at flow angularity.

From $\theta < 30°$ onwards, all three Bio-Inspired probes began to lose accuracy in total and dynamic pressure measurements. Pressure drop on novel probes L/D 0.5 and L/D 1.0 happens almost immediate after hitting flow angle of 30. For novel probe L/D 1.5, very small pressure drop happens throughout $10° < \theta < 30°$, huge pressure drop only occurs between flow angle of 35 and 40 degrees. Accuracy in total pressure measurement for the Bio-Inspired probe is a significant improvement to the conventional Pitot-static which suffers inaccuracy almost immediately. The conventional Pitot-static probe was only able to maintain an accurate total pressure measurement up to $\theta = \pm 10°$.

Total pressure loss at $\theta = 0°$ suffered by the Bio-Inspired probe with L/D 1.5 is at 80 Pa more than L/D 0.5, this remain unchanged when at wind speed of 90 ft/s and 115 ft/s. At wind speed of 90 ft/s, total pressure loss between novel probes L/D 0.5 and L/D 1.5 is reduced to 50 Pa.

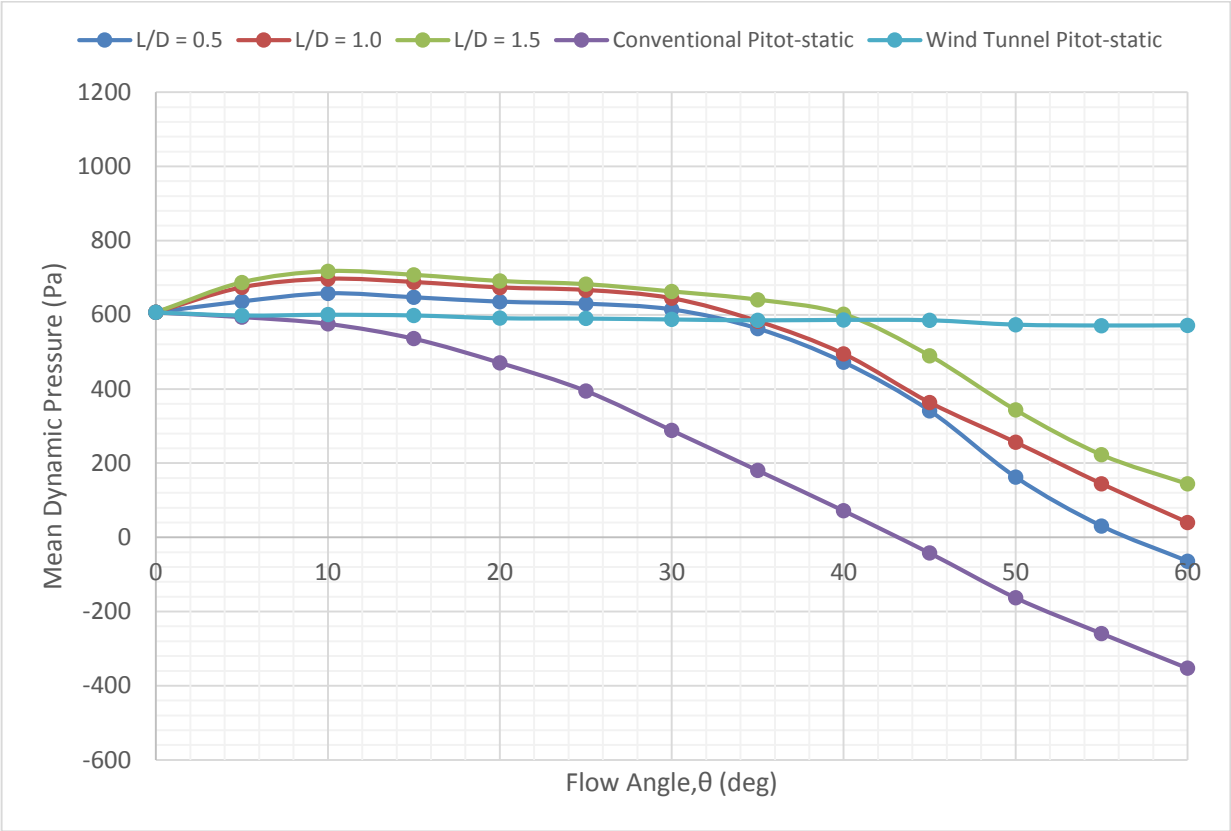

Figure 38: Calibrated pressure measurement at flow angularity of 4 probes at test section speed of 100 ft/s (30.5 m/s)

Overall, the Bio-Inspired probe L/D 1.5 was able to maintain the capture of dynamic pressure up to $\theta = \pm 40°$ before losing accuracy in pressure measurement. Novel probe L/D 0.5 and L/D 1.0, fair pretty close by maintaining dynamic pressure accuracy up to $\theta = \pm 35°$. L/D 1.5 has an increase of 400% in total pressure measurement after calibration. These results validates an early claim by Farokhi, Keshmiri and Taghavi[1], who also conducted wind tunnel test on the Bio-Inspired probe. The results also proves that longer protruding centerbody can maintain accurate total pressure measurement at high flow angle than shorter protruding body, a cost function study would be needed to optimize the protruding head.

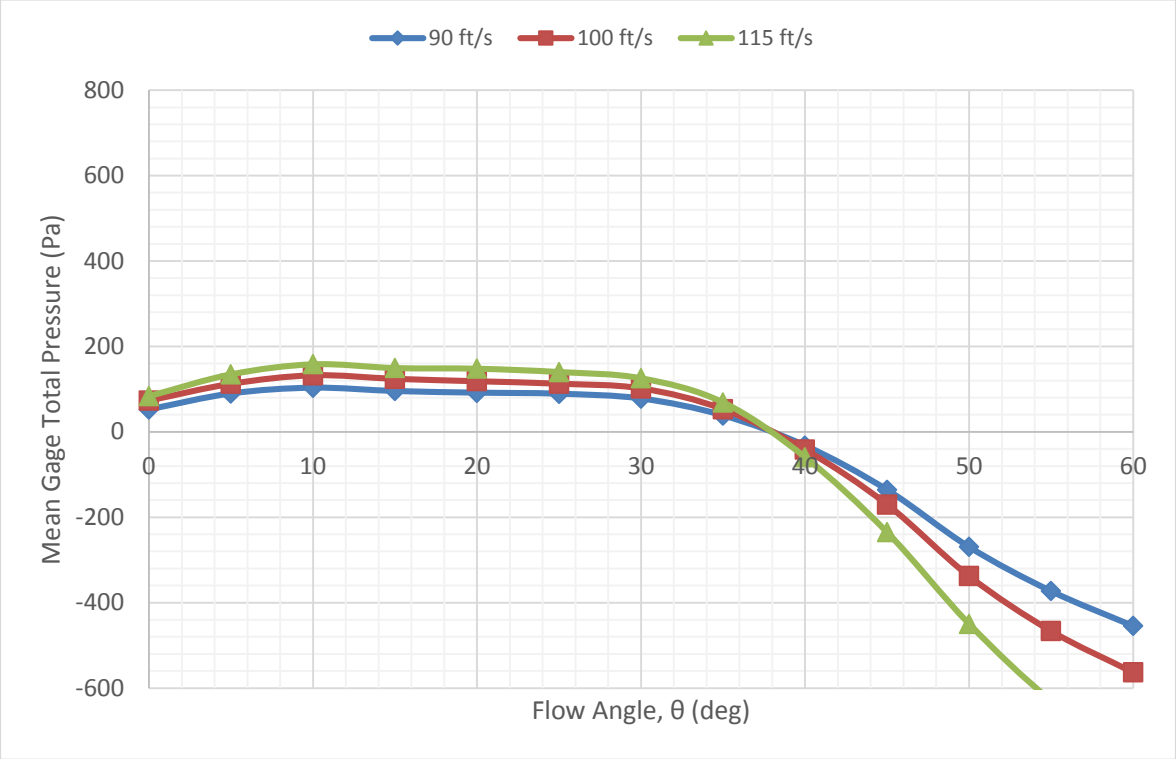

Figure 39: Gage total pressure measurement of Bio-Inspire L/D 0.5 at flow angularity

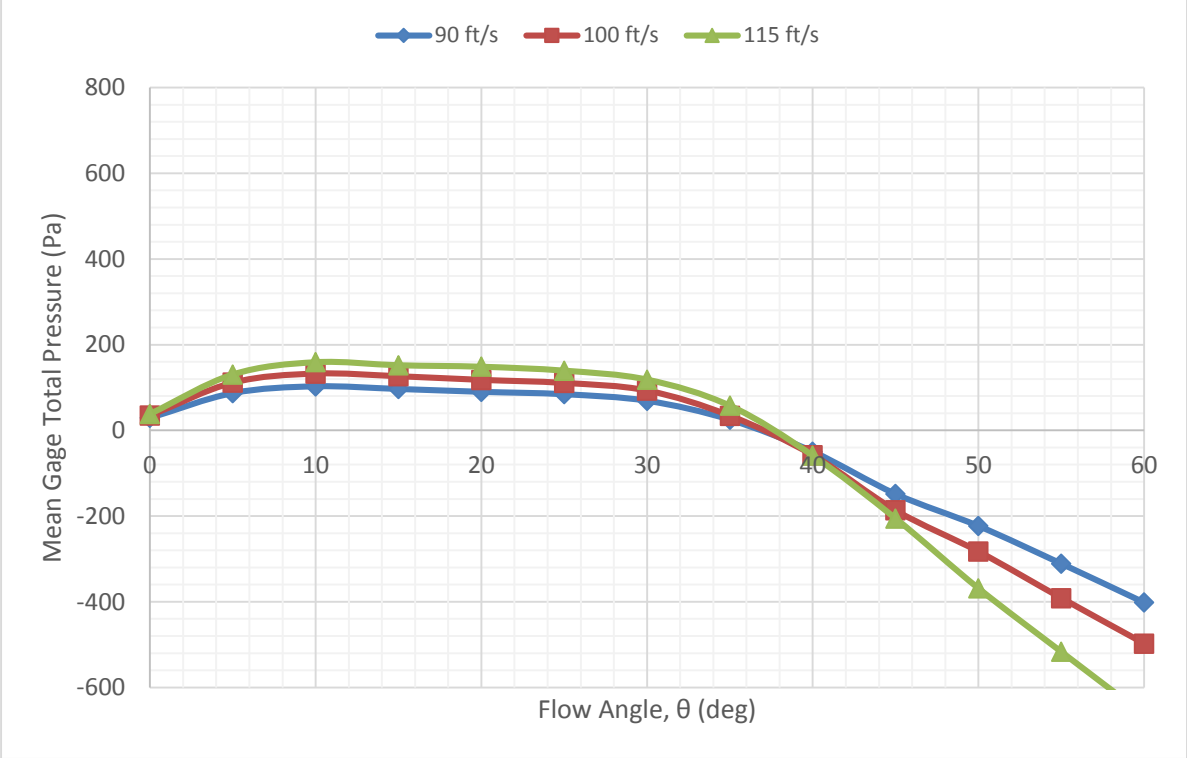

Figure 40: Gage total pressure measurement of Bio-Inspire L/D 1.0 at flow angularity

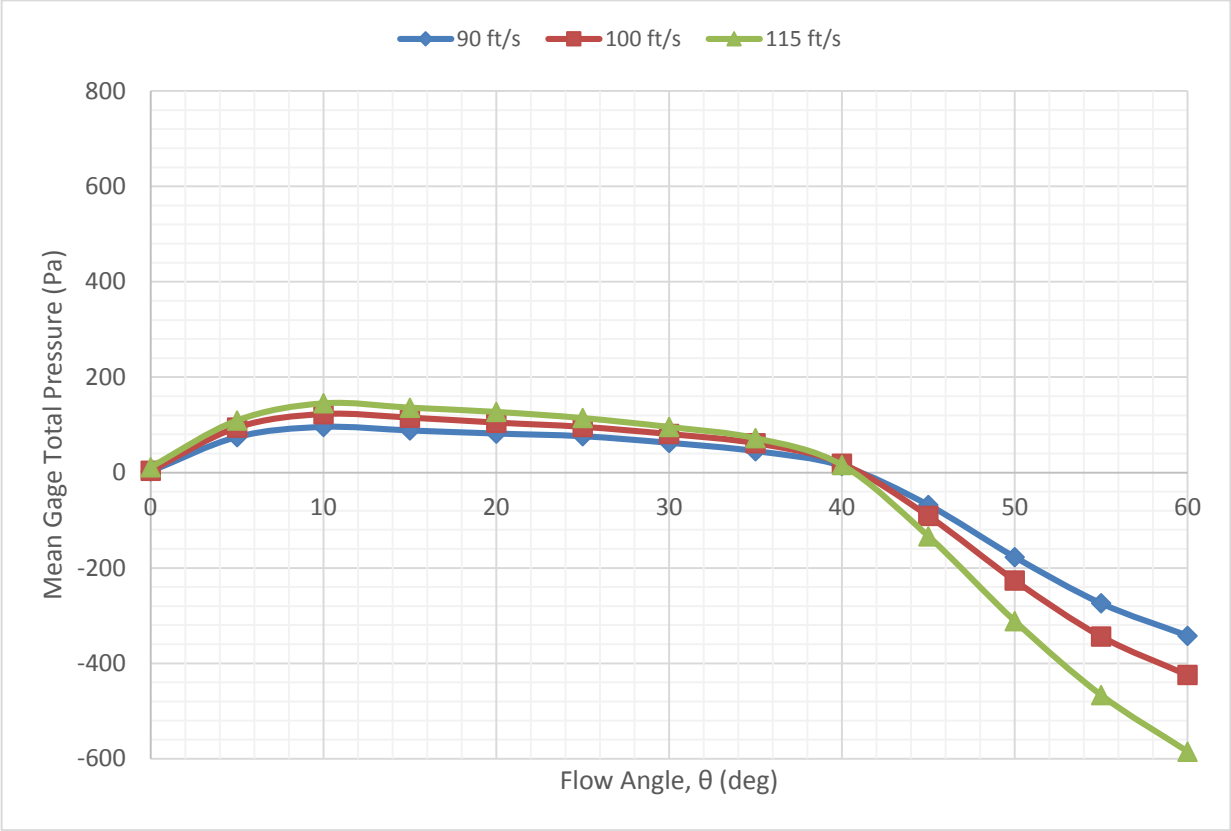

Figure 41: Gage total pressure measurement of Bio-Inspire L/D 1.5 at flow angularity

Figures 39 to 42 are the mean gage total pressure measurements of all four probes (L/D 0.5, L/D 1.0, L/D 1.5 and conventional Pitot-static tube) measured at wind speed, V of 90 ft/s, 100 ft/s and 115 ft/s. Observing these figures, total pressure loss at θ = 0°, $(\Delta p_t)_{C_{D0}}$ is largely unchanged at all three tested wind speed. Total pressure however starts deviating from the correct total pressure at a faster rate as wind speed increases. Total pressure drop rate begins to increase at θ = 30° for L/D 0.5 and 1.0, θ = 40° for L/D 1.5, and coming to a constant pressure loss rate through 40° < θ < 60°. Comparing between the novel probes with different protruding heads, L/D 0.5 suffered the highest dynamic pressure loss rate at θ < 40°. Table 1 present the mean total pressure loss rate flow angle above 40°.

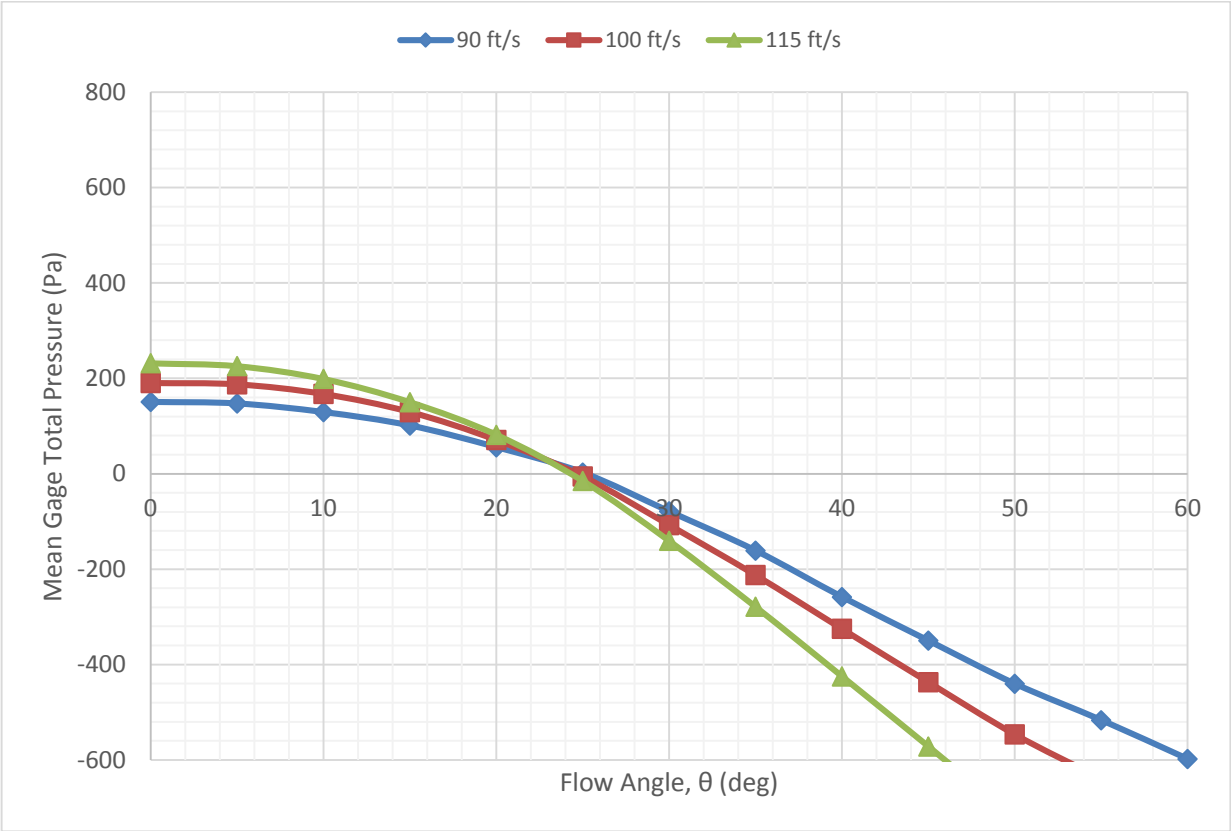

Figure 42: Dynamic pressure measurement of Conventional Pitot-static at flow angularity

Figure 42 shows the growing inaccuracy of the conventional Pitot-static probe with increase in speed. All novel probes are still able to measure accurate total pressure measurements up to flow angle of 40 degrees at wind speed of 115 ft/s. This shows that the Bio-Inspired probes will give a steady performance at higher speeds in maneuvering aircrafts.

Table 1: Total pressure drop rate at flow angle, θ < 40°

Probe	Wind Speed, V (ft/s)	Total Pressure Drop Rate (Pa/°)
L/D 0.5	115	39
	100	29.5
	90	23.7
L/D 1.0	115	31
	100	23.3
	90	17.5
L/D 1.5	115	32.6
	100	24.1
	90	19.2
Conventional	115	28.4
	100	21.8
	90	15.1

Novel Probe Protruding Head Optimization

Using the data from the wind tunnel experiments, the centerbody protruding head can be optimized to achieve minimum pressure deviation from the actual dynamic pressure in the wind tunnel. The following cost function, equation 10, with variable L/D and flow angle, θ is created. On equation 11, the constants, a, were determined using dynamic pressure, q results from wind tunnel experiment.

$$P_{est} = a_1\left(L/D\right)^2 + a_2\left(L/D\right) + a_3\left(\theta\right)^2 + a_4\left(\theta\right) + a_5\left(1\right) \qquad (10)$$

$$q = \begin{pmatrix} a_1 & a_2 & a_3 & a_4 & a_5 \end{pmatrix} \begin{bmatrix} \left(L/D\right) \\ L/D \\ \left(\theta\right) \\ \theta \\ 1 \end{bmatrix} \qquad (11)$$

A 3-D plot is then created from equation 10 on Figure 43.

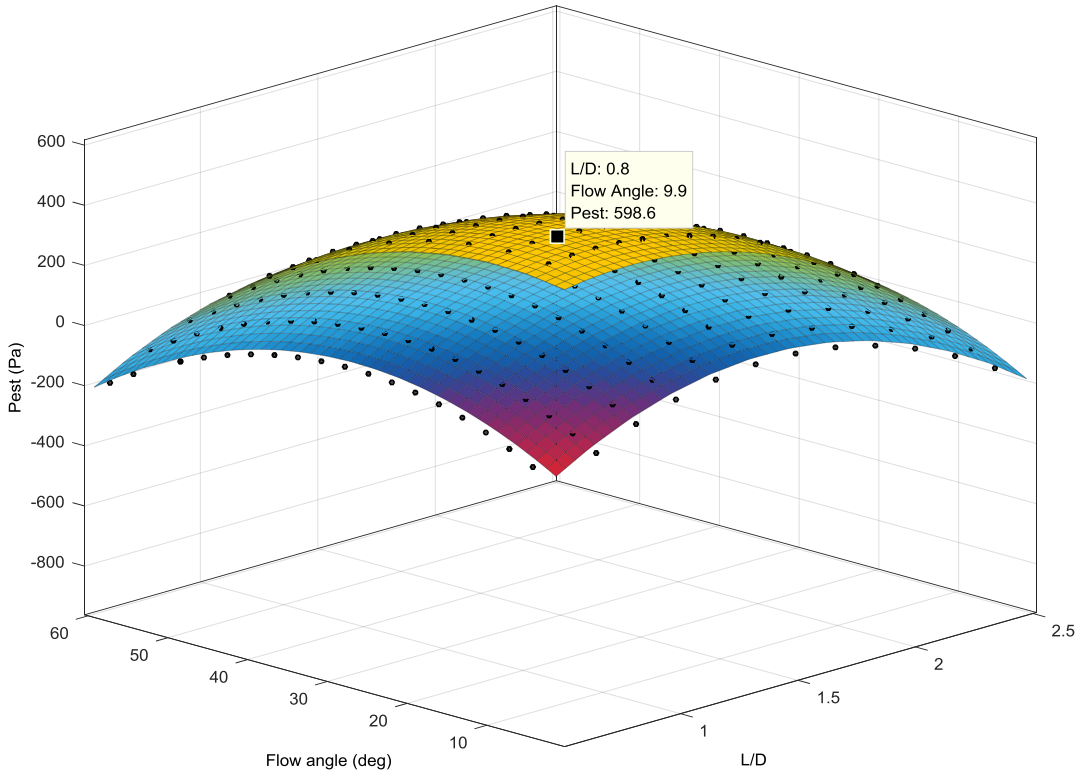

Figure 43: 3-D plot with L/D sweep

According to Figure 43, L/D 0.8 is the optimized protruding head size with minimum total pressure deviation. However pressure errors does exist in the estimated pressure, P_{est}, calculated from the cost function, thus angle sensitivity prediction is not accurate.

6 Conclusions and Future Works

6.1 Conclusions

Based on the results from both experimental wind tunnel tests and CFD analysis the following conclusion can be made:

- Flow remains attached to protruding centerbody at high flow angles as shown through computational analysis.
- The novel probe with L/D 1.5 protruding head accurately measures total pressure, Pt, up to $\theta = \pm 40°$ at wind speed of 90 ft/s and 100 ft/s. At higher wind speed of 115 ft/s, accurate total pressure measurement fell down to $\theta = \pm 35°$.
- L/D 0.5 and L/D 1.0, can accurately measures total pressure, Pt, of up to $\theta = \pm 30°$ at all three tested wind speeds.
- Conventional Pitot-static tube can only record accurate pressure up to $\theta = \pm 10°$ before losing accuracy in total pressure measurements.
- Wind tunnel results support L/D 1.5 ability to enhance accuracy of total pressure measurement at a higher flow angle compared to L/D 0.5 and 1.0, but incurs additional total pressure loss due to larger probe's centerbody C_D.
- All novel probes with different heads provided accurate total pressure measurements up $\theta = \pm 40°$. Proving that the novel probe will provide steady performance at high speeds in maneuvering aircraft
- Dynamic pressure measurements from wind tunnel tests validate computational results at flow angle of $0° < \theta < 40°$. At above 40°, computational results began to over predict the accuracy of dynamic pressure measurements. This occurrence is likely due to the

inaccuracy of turbulence models predicting swirl and flow separation on complex 3D geometry.

6.2 Future Works

Currently, research would be focused on flight testing all three Bio-Inspired probes on a UAS in a similar side-by-side configuration with a conventional Pitot-static tube. Additional wind tunnel testing will be conducted on a new Bio-Inspired probe to study direct drag measurement on the probe centerbody. Weight scale will be added into the hollowed centerbody of the bio-Inspired probe. This will allow direct drag measurements at all flow angles and allow direct feedback to the DAQ, enabling in flight calibration. Optimization of the probe's centerbody will continued.

7 References

1. Farokhi, S., Taghavi, R.R. and Keshmiri, S.S., "Bio-Inspired Airdata Sensing Probe for High Angles of Attack and Sideslip," *AIAA SciTech,* 53rd AIAA Aerospace Sciences Meeting, 5-9 January 2015, Kissimmee, Florida.

2. Russell W. R., Gracey W., Letko W., Fournier P. G., "Wind-Tunnel Investigation of Six Shielded Total-Pressure Tubes at High Angles of Attack – Subsonic Speeds," *National Advisory Committee for Aeronautics,* Technical Note 2530, Washington, November 1951.

3. Wikipedia, 'Peregrine falcon,' available: https://en.wikipedia.org/wiki/Peregrine_falcon

4. Panitz T., Wasan, D.T., "Flow Attachment to Solid Surfaces: The Coanda Effect," *AlChE Journal,* Vol. 18, Issue 1, January 1972, pp. 51-57.

5. Dean, B, Bhushan, B, "Shark-skin surfaces for fluid-drag reduction in turbulent flow: a review," *Philosophical Transactions of the Royal Society,* Journal, 2010.

6. Farokhi, S., Taghavi, R., Barrett, R. and Graf, G., "Pressure Drag Reduction Concepts in Maneuvering Submarine," *Invited Presentation*, 10th European Drag reduction Working Meeting, Berlin, Germany, March 19-20, 1997.

7. Larson, T.J., "Evaluation of a Flow Direction Probe and Pitot-Static Probe on the F-14 Airplane at High Angles of Attack and Sideslip," NASA Technical Memorandum 84911, March 1984.

8. Geenen, R.J., Moulton, B.J., and Haering, E.A., "A System for Testing Airdata Probes at High Angles of Attack using a Ground Vehicle," AIAA Paper No. AIAA-91-0088, Paper presented at the AIAA Aerospace Sciences Meeting, January 1991.

9. Space Age Air Data Products, Company website: [http://spaceagecontrol.com].

10. Whitmore, S., Moes, T.R. and Larsen, T.J., "High Angle of Attack Flush Airdata Sensing System," *Journal of Aircraft*, Vol. 29, No. 5, 1992, pp. 915-919.

11. Whitmore, S., and Cobleigh, B., "Stable algorithm for estimating airdata from flush surface pressure measurements," Publication Number: US6253166, 1998-10-05.

12. Nelson, L.D., Weimer, C.S., Caldwell, L.M., and O'Brien, M.J., "Optical air data measurement systems and methods, Application #CA 2494458 C, 2009.

13. Fourguette, D., "Molecular Air Data Clear Air Turbulence Sensor: MADCAT," *NASA TechPort Abstract,* 2010.

14. Mansour, M., Chokani, N., Kalfas, A. and Abhari, R.S., “Time-resolved entropy measurements using a fast response entropy probe,” *Measurement Science and Technology*, Vol. 19, 2008.

15. Schlicting H., Klaus G., “Boundary Layer Theory,” *Springer*, New York, 2000.

16. Holloway, D. S., Walters D. K., Leylek, J. H., “Predicition of unsteady, separated boundary layer over a blunt body for laminar, turbulent, and transitional flow,” *International Journal for Numerical Methods in Fluids,* 2004, pp. 1291-1315.

17. Sirangu V., Ng T.T., “Flow Control of a Slender Blunt-Nose Body at High Angles of Attack,” *Journal of Aircraft,* Vol. 49, No. 6, 2012, pp. 1904-1912.

18. El-Behery S. M., Hamed M. H., “A Comparative Study of Turbulence Models Performance for Turbulent Flow in a Planar Asymmetric Diffuser,” World Academy of Science, Engineering and Technology, 2009.

19. Cheng, G.C., and Farokhi, S., "On Turbulent Flows Dominated By Curvature Effects”, *ASME Journal of Fluids Engineering*, Vol. 114, March 1992, pp. 52-57.

20. Mani, M., Ladd, J. A., Bower, W. W., “Rotation and Curvature Correction Assessment for One- and Two-Equation Turbulence Models.

21. CD-Adapco, STAR-CCM+, Company website: [http://www.cd-adapco.com].

22. CD-Adapco, STAR-CCM+, manual, 2016.

23. Onoufriou, A., “Segregated or Coupled Flow,” Steve Portal, STAR-CCM+, Article 3626.